SYNTHESIS AND ELECTROCHEMICAL STUDY OF Pt- AND IrO_2- BASED NANOSTRUCTURED MATERIALS

A Thesis

Presented to

The Faculty of Graduate Studies

Lakehead University

By

KALLUM KOCZKUR

In partial fulfillment of the requirements

For the degree of

Master of Science

August 2006

Your file Votre référence
ISBN: 978-0-494-21514-2
Our file Notre référence
ISBN: 978-0-494-21514-2

Abstract

With ever increasing awareness that our environment is being ravaged at an alarming rate and the very seriously high rate of diabetes, there has been much research into understanding, controlling and reversing these processes. In my M. Sc. studies, the oxidation of methanol and glucose on Pt based nanomaterial electrodes has been examined while the electrochemical oxidation of white liquor has been studied on a nanostructured IrO_2-based electrode. Surface morphologies were characterized by scanning electron microscopy (SEM), energy dispersive X-ray spectrometry (EDS), and X-ray diffraction (XRD). Electrochemical analysis was performed by methods including cyclic and linear voltammetry (CV and LV), chronoamperommetry (CA), chronopotentiommetry, (CP), amperometric (i-t), and electrochemical impedance spectroscopy (EIS).

In an effort to improve several key aspects of the direct methanol fuel cell (DMFC), platinum and platinum based materials were studied as they are regarded as the most active anode catalyst for the DMFC. Novel three dimensional (3D) nanoporous Pt and PtRu network electrodes were successfully fabricated using electrochemical deposition and/or hydrothermal treatment. Surface analysis by SEM revealed the formation of the novel 3D nanoporous Pt and PtRu network electrodes. XRD spectra did not indicate a ruthenium peak which suggested that an alloy was formed. The active surface area of the samples measured by hydrogen adsorption/desorption in a 0.5 M H_2SO_4 solution indicated that the active surface area of the nanoporous Pt and PtRu electrodes was many times that of polycrystalline Pt. Electrocatalytic activity towards methanol oxidation was also studied by CV, CA, and EIS. Electrochemical experiments

showed a PtRu composition of 62/38 % had the best performance towards methanol oxidation with an activity over 100 times greater than that of polycrystalline Pt. Further studies of the PtRu nanomaterial electrodes were undertaken to evaluate their potential as non-enzymatic glucose sensors. Electrochemical oxidation of glucose was studied using a 0.1 M phosphate buffered saline (PBS, pH 7.4) solution with and without 0.15 M NaCl. CV experiments indicated a negligible effect of the chloride ion. Amperometry studies of the samples showed that steady state currents could be achieved in the range of 1-17 mM which contains the physiological range of glucose (3-8 mM). The electrode containing $Pt_{62}Ru_{38}$ exhibited superior sensitivity (as high as 0.022 mA/cm^2mM) and activity towards glucose detection despite the high concentration of the chloride ion.

Polysulfides have been reported to have generated up to a 1.8 % increase in pulp yield. Electrochemical treatment of white liquor is attractive because polysulfides can be produced in the anode compartment while caustic soda and pure hydrogen can be recovered in the cathode department. The IrO_2-based electrodes used in this study were Ti/Ta_2O_5-IrO_2 electrodes. Surface analysis indicated a typical "cracked mud" structure with oxide particles sitting on top of the electrode surface. White liquor in the kraft process is composed mainly of sodium sulfide, sodium hydroxide and sodium carbonate. The amplitude of the harmonic potential oscillations was between -150 mV and +750 mV/SCE. EIS studies were employed to study the origin of the oscillations during the electrochemical treatment of the white liquor and were classified as hidden negative differential resistance (HNDR) with oxygen evolution involved.

Acknowledgements

First off, I would like to thank my supervisor, Dr. Aicheng Chen, for all his help and guidance while pursuing my M. S.c. degree. His ideas and patience made the experience an enjoyable one. Also I would like to thank my committee members, Dr. Greg Spivak and Dr. Craig MacKinnon for their helpful suggestions.

Lab members, former and current, I would like to acknowledge include Brad Miller, Dan La Russa and Stephanie Nigro for their help in getting me started in the Chen lab. I would also like to thank Dr. Xinsheng Peng, Dr. Songqin Liu, Linda Bakovic, Dr. Qingfeng Yi, Dr. Min Tian, and Dr. Guosheng Wu for insightful discussions.

A special thank you goes to Debbie Leach and Ainsley Bharath for their help from the Chemical Stores room. Also, to Ed Drotar for his help in the Science Workshop, and Al MacKenzie, Ain Raitsakas, Jaili Wen, Keith Pringnitz and Dr. Ruslan Liferovich for their assistance in the L.U. Instrumentation lab.

Finally I would like to thank my parents for their constant support and encouragement.

Table of Contents

List of Symbols and Abbreviations

A	Ampere
AC	Alternating Current
Cdl	Double layer capacitance
CNDR	Coupled negative differential resistance
CA	Chronoamperometry
CP	Chronopotentiometry
CPE	Constant phase element
CV	Cyclic Voltammetry
DSA®	Dimensionally stable anode
E	Potential
EDS	Energy dispersive x-ray spectrometry
EIS	Electrochemical impedance spectroscopy
HB	Hoph bifurcation
HNDR	Hidden negative differential resistance
HS^-	Hydrosulfide
I	Current
ICE	Internal Combustion Engine
j	Current density
LGV	Linear galvanic voltammetry
NDR	Negative differential resistance
NP	Nanoporous

Rct	Charge transfer resistance
Rf	Resistance of the oxide film
SEM	Scanning electron microscopy
SCE	Saturated calomel electrode
T	Temperature
V	Voltage/potential
V vs SCE	Voltage vs saturated calomel electrode
XRD	X-ray Diffraction
Z_r	Real impedance
$-Z_i$	Imaginary impedance

Chapter 1

1. Introduction

Nanostructured materials possess some unique chemical and physical properties as well as a wide range of potential applications in catalysis [1,2], fuel cells [3,4] and chemical sensors [5,6], and an increasing importance in non-linear chemical dynamics studies. Fuel cells, and the catalysts which efficiently drive their reactions, form a critical field of study as finding a new power source to replace the internal combustion engine (ICE) is becoming increasingly important as global pollution levels from exhaust gases increase. Also, research into glucose sensors (blood sugar testing) for the purpose of controlling diabetes has received an enormous amount of attention recently due to the very high occurrence rate of the disease [7-10]. The interdisciplinary field of non-linear chemical dynamics has grown significantly in breadth and depth over the past two decades. Electrochemical reactions are attractive in non-linear dynamic studies as current and electrode potential can be easily monitored [11]. In the following sections, the application of Pt-based nanomaterials in fuel cells, the properties of enzymatic/non-enzymatic glucose sensing, non linear chemical dynamics and the electrochemical treatment of white liquor in the pulp and paper industry will be briefly summarized.

1.1 Nanostructured Pt-based Materials and Direct Methanol Fuel Cell

Air pollution, especially in large cities, is becoming an increasing cause of concern. Emissions from ICEs contribute significantly to the formation of photochemical smog, which is caused by the reaction of sunlight, nitrogen oxides (NOx) and volatile organic compounds (VOC) in the atmosphere. The primary source of NOx and VOC is the burning of fossil fuels.

For the moment, ICEs remain the only viable power source for vehicles. While batteries have seen an increase in use in hybrid vehicles, they are at a disadvantage for solely powering vehicles because of their limited energy storage capacity (100 – 150 Wh/kg) and the time necessary to recharge [12]. Fuel cells contain a specific power density on the order of 1 kWh/kg and a specific energy density in excess of 500 Wh. An example of such a fuel cell is the proton exchange membrane fuel cell (PEMFC). The best fuel for this system is hydrogen, with a high energy density of 33 kWh/kg; however, hydrogen has refueling, storage and handling limitations which still need to be addressed [13,14]. Alcohols, especially methanol, are promising fuel sources since they are easy to handle and burn cleanly.

Nanomaterials have unique properties and characteristics compared to bulk compounds. Since nanostructured materials have a large surface area, they could enhance applications which involve adsorption, such as fuel cells, chemical detectors and catalysts when compared to the traditional bulk materials. One application which has garnered a significant amount of interest is the Direct Methanol Fuel Cell (DMFC), which possesses the ability to overcome the purity and storage constraints of a hydrogen fuel cell [15]. The DMFC has strong potential to replace ICEs in that the theoretical efficiency is 96.7 % and the theoretical energy density is 6.09 kWh/kg [16]. Internal to the cell, at the anode, the direct electrochemical oxidation of methanol proceeds according to the following reaction [12,17]

$$CH_3OH_{(l)} + H_2O_{(l)} \rightarrow CO_{2(g)} + 6H^+_{(aq)} + 6e^- \qquad 0.016 \text{ V/SHE} \qquad (1.1)$$

The reduction of oxygen occurs at the cathode according to the following reaction:

$$O_2 + 4H^+ + 4e^- \rightarrow 2H_2O \qquad 1.229 \text{ V/SHE} \qquad (1.2)$$

Thus, the overall methanol oxidation reaction can be written as:

$$CH_3OH + 3/2O_2 \rightarrow CO_2 + 2H_2O \qquad 1.245\ V/SHE \qquad (1.3)$$

Some concerns with this fuel cell technology involve the crossing over of methanol through the Nafion® membrane [18], and the partial oxidation of methanol. This partial oxidation leads to an increased anodic overpotential as well as the formation of CO. The CO is absorbed onto the catalyst, thereby causing a substantial reduction in efficiency to approximately 27 % [16]. This, in part, has prompted extensive research into finding a catalyst which minimizes the poisoning effect of CO.

To avoid the formation of carbonate, DMFCs are run in an acidic medium. The ionic membrane is acidic in nature and may lead to the corrosion of the electrode materials. Ruthenium is currently recognized as the best second metal for this application, exhibiting stability in the potential range in which a DMFC operates, as well as shifting the oxidation of methanol to lower potentials when coupled with platinum [12]. Platinum and ruthenium are stable in acid, have good electrocatalytic activity and can oxidize methanol, CO and other intermediate species.

Essential to the electro-oxidation of methanol is a platinum based catalyst, but platinum suffers from the effects of poisoning intermediate species [19]. This is illustrated in the following reactions [12,17,20]:

$$Pt(s) + CH_3OH \rightarrow Pt\text{-}CH_2OH + H^+ + e^- \qquad (1.4)$$

$$Pt\text{-}CH_2OH + Pt(s) \rightarrow Pt_2\text{-}CHOH + H^+ + e^- \qquad (1.5)$$

$$Pt_2\text{-}CHOH + Pt(s) \rightarrow Pt_3\text{-}COH + H^+ + e^- \qquad (1.6)$$

$$Pt_3\text{-}COH \rightarrow Pt\text{-}CO_{ads} + 2Pt(s) + H^+ + e^- \qquad (1.7)$$

Therefore platinum is usually accompanied by a co-catalyst. Platinum-ruthenium alloys have shown the best results thus far [21-24]. With the presence of Ru, the adsorbed OH groups lead to the oxidation of CO at much lower potentials than for polycrystalline Pt. Also Ru can potentially oxidize the $-COH_{ads}$ directly into carbon dioxide without forming the CO poisoning species based on the following reaction mechanism [12,17,20]:

$$Pt + H_2O \rightarrow Pt\text{-}OH_{ads} + H^+ + e^- \quad (1.8)$$

$$Ru + H_2O \rightarrow Ru\text{-}OH_{ads} + H^+ + e^- \quad (1.9)$$

$$Pt\text{-}CO_{ads} + Ru\text{-}OH_{ads} \rightarrow Pt + Ru + CO_2 + H^+ + e^- \quad (1.10)$$

$$Pt\text{-}CO_{ads} + Pt\text{-}OH_{ads} \rightarrow 2Pt + CO_2 + H^+ + e^- \quad (1.11)$$

$$Pt\text{-}COH_{ads} + Ru\text{-}OH_{ads} \rightarrow Pt + Ru + CO_2 + 2H^+ + 2e^- \quad (1.12)$$

There are two proposed mechanisms of the enhancement of Pt's catalytic activity by Ru. One is the ligand effect mechanism, where the electronic properties of Pt are modified by a Pt-Ru orbital overlap [25]. The other is the bifunctional mechanism: Ru stimulates the chemisorption of methanol at lower potentials by providing a number of kinetically facile sites for chemisorption. However, at room temperature, the increasing Ru concentration leads to a decrease in the final surface coverage of methanol. Also, Ru is oxidized at significantly lower potentials than Pt. Surface species of $Ru\text{-}OH_{ads}$ can promote the oxidation of chemisorbed fragments to CO_2. When Ru coverage is low, the rate limiting step seems to be the migration of CO_{ads} to $Ru\text{-}OH_{ads}$, but when Ru coverage is high, oxidation of CO_{ads} is the rate limiting step [26]. Several methods have been developed to optimize the preparative method [27], surface distribution [28], particle size [29], and oxidation state [24] of the Pt and Ru. In order to reduce the cost of the DMFC, the catalyst's noble metal coating load needs to be significantly reduced. Supporting Pt and

PtRu nanoparticles on high surface area carbon supports improve catalyst utilization [30]. Unsupported PtRu colloids and PtRu/carbon nanomaterials have been prepared by several methods, including single/dual source molecular precursors, solution phase reduction of metal ions and thermal decomposition [31,32]. Carbon blacks, desulfurized carbon blacks, fullerene soot and Vulcan carbon powder have been used as carbon supports [33]. A support material with high surface area is required to get high performance such as high surface area carbon black; however, carbon black can not function alone due to its powder phase. Another support material is needed to immobilize carbon black so it is suitable for practical applications. A self-supported substrate for direct immobilization of Pt, PtRu nanoparticles and Pt, PtRu 3D nanoporous networks is desirable for a large surface area and high performance electrode. Ideally, the optimum surface composition should match the number of Pt-Ru pair sites with the optimal surface of the methanol molecule.

1.2 Diabetes and Non-Enzymatic Glucose Sensing

Currently there is an enormous interest in developing precise and quick methods to monitor blood sugar levels for the purposes of controlling and treating diabetes [7-10,34]. The current world market for biosensors is dominated by glucose biosensors (approximately 85 %) [35]. There are numerous reasons for this, but the single most prevalent is the alarming rate of diabetes in developed countries [35]. In Canada it is currently estimated that over 2 million Canadians have the disease [36]. Diabetes occurs in two forms, diabetes insipidus and diabetes mellitus. Diabetes insipidus is a disease characterized by excessive amounts of dilute urine. Diabetes mellitus is a medical disorder characterized by varying or persistent

hyperglycemia (high blood sugar levels) resulting from inadequate secretion of the hormone insulin from the pancreas [37]. There are two types of diabetes mellitus. Type 1 diabetes (juvenile diabetes) occurs when little to no insulin is secreted from the pancreas. This accounts for appoximately 10 % of diabetics. Regular insulin injections are almost always necessary for survival. Type 2 diabetes, most often affecting the middle aged and elderly is the more common form affecting 90 % of diabetics. It is caused when the body either doesn't use the insulin produced effectively or insufficient quanties are produced . Type 2 diabetes is much more managable and can often be kept under control by exercise and dieting, oral medication and self monitoring [35]. Self monitoring is very important as it provides data on the impact of diet, medicine, exercise, glucose control, alterations to treatment plans and possible factors that may be responsible for low/high glucose levels. If oral medication proves ineffective or has negative side effects insulin injections may be used. Diabetes is well documented as one of the leading causes of death. According to the American Diabetes Association, diabetes has been linked to increases in heart disease, greater than 60 % of all non-traumatic limb amputations, adult blindess, as well as serious kidney disease.

The current apex of diabetes mellitus treatment would be the introduction of an artificial pancreas coupled with a subdermal glucose sensor. Continuous readings of glucose levels would be accomplished by the sensor, while the artificial pancreas would provide insulin production as necessary. Currently, this approach is impractical due to several issues, the most prevalent being bio-incompatibility, and the rejection of the sensor by the body. A much less invasive method which has received significant attention recently is the use of external electrochemical biosensors for glucose detection [35]. They produce quick, concise readings using a disposable tip, which eliminates the possibility of instrument contamination.

Several studies have been conducted to counter the drawbacks of enzymatic glucose sensing [5,6,38]. Electrochemical biosensors for glucose, quite commonly glucose oxidase (GOx), are usually immobilized onto electrodes by covalent attachment, entrapment within a film or by passive adsorption. However, the corresponding enzyme-bound electrodes are susceptible to denaturing as well as poor sensitivity and stability. Although the oxidase enzyme is inexpensive, the co-substrate, oxygen, gets depleted as the sample gets used, resulting in decreased performance. Temperature, chemical and thermal instability, pH and humidity (while in storage or in use) have also been shown to be other potentially damaging factors to enzymatic sensors [38]. In addition, the poisoning of the electrode surface by the chloride ion, which is present under physiological conditions (0.1 M), remains a problem for glucose biosensors. An electrode which is capable of sustaining sensitivity and stability under physiological glucose levels (3-8mM) is desirable. Nanostructured Pt materials have great potential for non-enzymatic glucose detection due to their excellent electrocatalytic properties. Several methods have been developed for the preparation of nanostructured Pt [39-41]. Non-enzymatic sensors are also attractive for their simplistic fabrication and ease of regeneration. This includes methods which utilize mesoporous platinum as well as template directed synthesis for producing platinum nanotubules.

Amperometric studies are an important testing process for glucose sensing. Two important considerations are the mechanism of glucose oxidation on a platinum electrode and the electrocatalytic oxidation of glucose. The mechanism of glucose oxidation on a platinum electrode was first reported in 1985 by Vassilyev et al.[42]; however, further studies are required for a better understanding. One conclusion that was derived from these results was that the kinetically controlled glucose oxidation was too slow, which lead to insufficient

sensitivity, selectivity and faradaic current. Uni-metallic metals, of which platinum is currently the leading choice, do not exhibit good sensitivity to glucose. In a phosphate buffer, using a platinum electrode with a roughness factor of 2.6, the sensitivity at 6 mM glucose has been reported to be 0.14 $\mu A/cm^2$ [38]. To counter this, studies to enhance the electrocatalytic activity and sensitivity towards glucose oxidation have been conducted using platinum based alloys, including Bi, Pb, Pd, Tl and WO_3 [34,43,44]. These alloys, however, suffer from the toxicity of heavy metal elements, which prevents them from being put into practical applications. Platinum-lead alloy electrodes have been shown to oxidize glucose at negative potentials, which is the cause of their insensitivity to interfering species such as L-ascorbic acid (AA), 4-acetamidophenol (AP) and uric acid (UA). Although the physiological levels of these interfering species are low (0.1 mM AA, 0.1 mM AP, and 0.02 mM UA), they produce oxidation currents comparable to highly concentrated glucose because their electron transfer rates are substantially faster than that of glucose oxidation. The Pt_2Pb electrode is however susceptible to poisoning by the chloride ion. In the presence of 0.01 M NaCl, the amperometric signal decreases quickly and nearly disappears altogether.

1.3 Electrochemical Oscillators

The initial observation of electrochemical reactions producing variations in current or potential was first published in the early part of the 20^{th} century [45]. Since that time, a variety of electrochemical oscillators have been discovered during the anodic oxidation of ethylene and formate [46], formaldehyde [47], formic acid [48-50], methanol [51] and hydrogen [52], as well as in the anodic dissolution of metals including Sn, Fe, Zn, Cu and Ni [51,53]. Oscillations during the cathodic reduction of hydrogen peroxide [54] and iodate

[55,56] on single or polycrystalline platinum electrodes have also been observed. Details on non-linear behavior in electrochemical reactions can be found in several recent reviews [11,57-59]. For an oscillation to occur, a potential region of negative slope must contain two values for U (applied constant potential) and R (uncompensated ohmic resistance) for which the dynamics show two stable states on positive sloping branches and one unstable state on the negative branch (bistability) [60]. Bistability may occur when the system is in one of two stable stationary states, for instance, one at low current density, the other at high current density, when the bistability is generated by a positive feedback loop (mechanistically self-enhancing step). When a second feedback loop behaving in a negative manner is present, oscillations may also occur. Oscillations themselves were initially classified as chemical or electrochemical oscillation [61]. Near the end of the 20^{th} century, Koper proposed a new classification system based on impedance spectra and experimental control mode [62]. The classes of oscillators cited included those under potentiostatic conditions, potential static conditions with a large ohmic drop, and galvanostatic conditions with a large ohmic drop [63]. In the present work, for the first time, we report on potential oscillations during the electrochemical treatment of white liquor from the pulp and paper kraft process. Of interest to us was the third class of oscillators proposed by Koper which have since been expanded to negative differential resistance (NDR) and hidden negative differential resistance (HNDR) oscillators. NDR oscillators occur in the absence of chemical instabilities and current oscillations occur only on the negative slope of a stationary I/Φ profile [64]. A chemical species forms the slow negative feedback with Φ being autocatalytic. HNDR oscillators form under conditions similar to NDR; however, they also contain galvanostatic potential oscillations, which operate on a brief time scale and are hidden on an I/Φ curve [62]. Current

oscillations contained within HNDR oscillators have a positive zero frequency impedance as well as a Hopf Bifurcation (HB) associated with them. The HNDR class of oscillator has been further expanded upon to take into account the effects of mass transport/convection [55,56]. Li et al.'s work on oscillations during iodate reduction in alkaline solutions dealt with the effect of periodic gas evolution on the potential oscillations. They proposed the diffusion controlled depletion of iodate on the electrode surface involving a pair of overlapping positive and negative feedback loops and the convection induced replenishment of iodate by periodic hydrogen evolution to account for the potential oscillations.

1.4 White Liquor Chemistry

White liquor is composed mainly of sodium sulfide, sodium hydroxide and sodium carbonate. The presence of polysulfide in white liquor is known to increase the pulp yield and improve the paper quality in the kraft process. Sulfide in white liquor is used to remove the lignin from wood fibres; however, sulfide can also degrade the cellulose and hemi-cellulose chains (the Peeling Reaction). Polysulfides are important because they prevent the beta alkoxy elimination reaction from occurring. The terminal ends of the cellulose and hemi cellulose chains are oxidized to prevent their degradation. Polysulfide can be commercially produced within white liquor using air-oxidation methods, for instance the MOXY™ process [65]. The MOXY™ process consists of two parallel anthrasite filters and reactors. White liquor is pumped into the reactors and is partially oxidized with air in the presence of a carbon catalyst [66]. However, the air-oxidation method has some drawbacks due to the formation of thiosulfate (inert cooking chemical) as a useless by-product and polysulfide decomposition to thiosulfate at high temperatures limiting the polysulfide concentration. In

contrast, electrochemical oxidation of white liquor can generate highly concentrated polysulfide liquor, showing great potential for application in the pulp and paper industry [67-69]. Sulfide in white liquor is easily oxidized to form polysulfides in the anode compartment at low electrode potential [70-71]:

$$S^{2-} \rightarrow S + 2e^- \qquad E / V \text{ vs SCE } -0.508 \qquad (1.13)$$

$$HS^- + OH^- \rightarrow S + H_2O + 2e^- \qquad E / V \text{ vs SCE } -0.478 \qquad (1.14)$$

$$2S^{2-} \rightarrow S_2^{2-} + 2e^- \qquad E / V \text{ vs SCE } 0.238 \qquad (1.15)$$

$$S^{2-} + S_2^{2-} \rightarrow S_3^{2-} + 2e^- \qquad E / V \text{ vs SCE } 0.248 \qquad (1.16)$$

$$S^{2-} + S_3^{2-} \rightarrow S_4^{2-} + 2e^- \qquad E / V \text{ vs SCE } 0.278 \qquad (1.17)$$

Pure hydrogen is produced as a by-product on the cathode. Pure sodium hydroxide is also recovered in the cathode compartment when a membrane is used to separate the anode and the cathode. Therefore, polysulfide and caustic soda, two very useful chemicals, are produced simultaneously during the electrochemical treatment of white liquor.

On the other hand, electrochemical oxidation of aqueous sulfide has garnered significant attention for the detection and removal/conversion of the highly toxic sulfide species [72]. The electrochemical behavior of sulfide has been investigated using different electrode materials, including platinum [67,73,74], graphite [68], gold [75], IrO_2-based mixed oxides [76,77], and HgTe semiconductors [78]. The formation of a sulfur layer on the electrode surfaces as well as the production of polysulfides in solution has been observed during the anodic oxidation of sulfide. Oxyanions of sulfur, for instance, thiosulfate and sulfate, can also be formed. However, the mechanisms of sulfide oxidation and soluble polysulfide ions formation, and the nature of the deposited sulfur still need to be clarified. Thus, further investigation of sulfide oxidation and the electrochemical treatment of white

liquor are critical to remove effectively sulfide from wastewater streams, and to convert economically sulfide into polysulfide for application in the kraft pulping process.

1.5 Scope of the Thesis

In this study, we investigated the effects enhancing Pt and Pt-based electrodes by increasing the surface area and activity by the formation of 3D nanoporous networks on Ti substrates. Chapter 2 will elaborate on the electrochemical deposition/hydrothermal electrode fabrication procedures and surface analysis techniques such as scanning electron microscopy (SEM) and electrochemical methods used to characterize the nanostructured materials. Chapter 3 will present findings for the activities of nanostructured Pt materials on a Ti substrate towards methanol oxidation. Chapter 4 will detail results of the effect of different Ru concentrations on the electrocatalytic performance of nanoporous Pt materials and the non enzymatic oxidation of glucose. Chapter 5 will present potential oscillations during electrochemical treatment of white liquor on a nanostructured Ti/Ta_2O_5-IrO_2 electrode including the proposed mechanism of the observed oscillations. Chapter 6 will provide a summary of the results and conclusions.

Chapter 2

Experimental Section

2.1. Electrode Fabrication

2.1.1. Nanoporous 3D Pt Nework Electrodes

Three Dimensional (3D) nanoporous platinum network electrodes were successfully fabricated in this study. Titanium foil was washed with acetone followed by Nanopure water (18.2 MΩ cm). The Ti foil was then etched with 18% HCl at 85°C for 10 minutes to remove the thin oxide layer on the titanium surface. Platinum nanoparticles were electrodeposited on the Ti substrate at -20 mA/cm^2 for 3 minutes from a solution composed of $H_2PtCl_6 \cdot 6H_2O$ and HCl. The treated Ti substrate was then transferred into a Teflon® lined autoclave containing ethylene glycol (EG), $H_2PtCl_6 \cdot 6H_2O$ and HCl. Hydrothermal assisted reduction (at 100°C for 10 hours) was used for the formation of the nanoporous (NP) Pt networks on the Ti substrate. After cooling to room temperature, the sample was washed again with Nanopure water and acetone.

2.1.2. Nanoporous 3D PtRu Network Electrodes

Ruthenium nanoparticle colloids were synthesized from a deaerated aqueous solution containing $RuCl_3 \cdot 3H_2O$, citric acid and $NaBH_4$ at room temperature. Titanium foil pieces with 3D NP Pt networks on their surface were transferred to a Teflon® autoclave with 10 mL of Ru nanoparticle colloid solution and heated at 100°C for 10 hours. After cooling to room temperature, the samples were washed again with Nanopure water and acetone and then dried. A calcined process was applied to the samples under

argon protection at 200°C. By altering the concentration of the Ru colloid solution, nanoporous PtRu electrodes with varying ratios of Ru were prepared.

2.1.3. High Performance 3D PtRu Alloy Electrodes

A simplified procedure was used to produce high performance nanostructured PtRu alloy electrodes. The 3D nanoporous PtRu alloy network electrodes were fabricated using the following procedure. First, pieces of titanium foil were washed with Nanopure water (18.2 MΩ cm), then etched with an 18% HCl solution at 85°C for 10 minutes to remove the oxide layer on the titanium surface. The etched substrate pieces were transferred to a Teflon® autoclave containing formaldehyde, $H_2PtCl_6 \cdot 6H_2O$, $RuCl_3 \cdot 3H_2O$, and HCl and heated at 180°C for 10 hours. After cooling to room temperature, the coated substrates were removed, air dried, then rinsed with Nanopure water.

2.1.4. Ti/Ta_2O_5-IrO_2 Anode

The working electrode Ti/Ta_2O_5-IrO_2 was prepared using the thermal decomposition technique. The Ti substrates were first degreased using acetone, washed with distilled water, and then etched with 32% HCl at approximately 85 °C for 15 minutes. The coating solution was made by mixing an iridium precursor solution and a tantalum precursor solution. The mixture of precursor solutions was painted on the pretreated Ti substrate; the solvent was evaporated at around 80 °C by an air stream and then calcinated at 500 °C for 10 minutes. This procedure was repeated until the oxide

coating load reached around 25.0 g/m^2. A final one hour post-baking at 530°C completed the procedure.

2.1.5. Pt Wire/Pt Coil (Counter Electrode)

The platinum wire utilized as a working electrode had a 1.0 cm^2 surface area and was flame annealed and quenched using Nanopure water prior to experimentation. The counter electrode, also platinum wire, had a surface area of 10 cm^2 and was flame annealed and quenched with Nanopure water prior to experiments.

2.2. Surface Analysis

Analysis of the substrate and coatings was carried out using scanning electron microscopy (SEM) and energy dispersive X-ray spectrometry (EDS) (JEOL 5900LV instrument). X-ray diffraction (XRD) analysis was performed using a Phillips PW 1050-3710 Diffractometer.

2.3. Solution Preparation

The electrolytes were made with H_2SO_4 (Aldrich, 99.999%), methanol (Caledon, 99.9%), KH_2PO_4 (Aldrich, 99.0%), K_2HPO_4 (Aldrich, 99.0%), NaCl (Anachemia, 99.0%), glucose (BDH, analytical grade) and pure water (Nanopure, 18.2 MΩ cm). Carbon monoxide (PRAXAIR, 99.9%) was used for the CO study. Ultrapure argon (BOC GASES, 99.999%) was used to deaerate all solutions prior to measurements, and passed over top of the solution during testing. All measurements were conducted at room temperature.

2.4. Electrochemical Experiments

The three electrode cell system used in this study has been previously described [79]. Electrochemical techniques such as cyclic voltammetry (CV), linear galvanic voltammetry (LGV), chronoamperommetry (CA), and chronopotentiommetry (CP) were performed using a Solartron Analytical SI 1287 electrochemical interface with data acquisition accomplished with Corrware electrochemical software. Data acquisition and analysis for the glucose sensing studies was done with a CH Instruments CHI660B potentiostat. An Orion Research model SA 250 was used to measure the pH of the investigated solutions. Temperature experiments were completed using a Fisher Scientific water bath. Electrochemical Impedance Spectroscopy (EIS) was performed with a Solartron Analytical 1252A frequency response analyzer in conjunction with the 1287 electrochemical interface. Zplot electrochemical software was used to acquire the impedance data. Unless otherwise stated, the amplitude of the AC modulation potential is 10 mV and the frequency range selected was 40 kHz to 40 mHz.

2.5. Electrochemical impedance spectroscopy

All discussions involved in this section will be restricted to simple circuits to simplify the mathematics involved. Ohm's law, which can be expressed as

$$E = IR \tag{2.1}$$

where E is the potential, I is the current and R is the resistance. If we consider AC signals the sinusoidal voltage can be expressed using the angular frequency

$$e = E \sin\omega t \tag{2.2}$$

where ω is the angular frequency and is 2π times greater than the conventional frequency [80]. It is normally best to consider the voltage as a phasor quantity so that the observed potential at any time t is a component of the amplitude E and the frequency of rotation ω [80]. To compare related sinusoidal signals (AC potential and current), they can be expressed as separate phasors rotating at the same frequency that are not normally in phase (i.e., separated by a phase angle ϕ). If the phasor E' is the reference signal and ϕ is measured with respect to it then the current can be expressed as

$$i = I \sin(\omega t + \phi) \tag{2.3}$$

If the frequency is constant, this allows the rotation component to be dropped from phasor diagrams and the phasors can be expressed as vectors with a common origin and separated by the appropriate angles [80].

Applying this information to simple circuits, a pure resistance with a sinusoidal voltage applied of $e = E\sin\omega t$, the current can be expressed as $I = (E/R)\sin\omega t$ due to Ohm's law, or in terms of phasor notation

$$I' = E'/R \tag{2.4}$$

If a pure resistor is replaced with a pure capacitance, then the current can be written as

$$i = \omega CE\cos\omega t \tag{2.5}$$

or

$$i = (E/X_c)\sin(\omega t + \pi/2) \tag{2.6}$$

where the capacitive reactance (X_c) is equal to $1/\omega C$. In this case the phase angle is now $\pi/2$ as opposed to 0 for the case of a pure resistance, and the current now leads the voltage [80]. At this point it is best to include the idea of complex notation to express phasors and they are multiplied by $j = \sqrt{-1}$. Even though the current's phase angle is

measured with respect to the voltage, the voltage phasor E' can still be expressed for a pure capacitance

$$E' = -jX_cI' \tag{2.7}$$

where $-jX_c$ takes the place of the resistance in Ohm's law [80].

At this point, a simple circuit can be constructed with a pure resistance and pure capacitance in series with a voltage (E') applied which must equal the sum of the voltage drops across each component which means that

$$E' = E'_R + E'_C \tag{2.8}$$

$$E' = I'(R-jX_c) \tag{2.9}$$

$$E' = I'Z \tag{2.10}$$

This expression allows for the link between voltage and current through Z which is called the impedance and is equal to: $R - jX_c$. Generally the impedance is expressed as

$$Z(\omega) = Z_{Re} - jZ_{Im} \tag{2.11}$$

where $Z_{Re} = R$ for a pure resistance and $Z_{Im} = 1/\omega C = X_c$ for a pure capacitance and the magnitude of the impedance is

$$|Z|^2 = (Z_{re})^2 + (Z_{Im})^2 \tag{2.12}$$

Another method for the analysis of AC circuits is the idea of admittance (Y). Admittance is simply the inverse of impedance and in some cases may be easier to work with since procedures used to model circuits often involve the conversion of a series circuit to a parallel circuit and vice versa [81]. With this in mind admittance can be expressed as

$$Y = 1/Z = Y_{Re} + jY_{Im} \tag{2.13}$$

and can also allow Ohm's law to be rewritten as

$$I' = E'Y \quad (2.14)$$

This is a useful term when considering parallel circuit elements since the overall admittance is simply the sum of the individual admittance elements [80].

2.5.1 Equivalent circuits

To understand the behavior of an electrochemical system from an impedance standpoint it is often useful to express the resulting impedance in the form of an equivalent circuit. The equivalent circuit is an electrical representation of the behavior of the system at different potentials or currents. Table 2.1 is comprised of the available elements that can be used in the construction of an equivalent circuit [82].

Notation	Identification	Notation	Identification
R	Resistance	C	Capacitance
CPE	Constant Phase Element	W	Warburg Element (Diffusion)
L	Inductance	T	Tangent Hyperbolic (Diffusion)
G	Gerischer Impedance	O	Cotangent Hyperbolic (Diffusion)

Table 2.1: Available elements for equivalent circuits.

The simplest electrochemical cell essentially behaves like a resistor in series with a capacitor and can be expressed as shown in Figure 2.1, where Rsol and Cdl represents the resistance of the solution and capacitance of the double layer respectively [82].

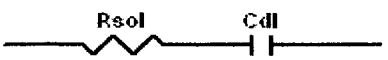

Figure 2.1: Equivalent circuit representation of a simple electrochemical cell.

When a faradaic process occurs at the electrode, there is the generation of a faradaic impedance that is in parallel with the double layer and if the reaction is irreversible, then the faradaic impedance can be considered as a pure resistance and is called the charge transfer resistance and can be reflected in the revised equivalent circuit shown in Figure 2.2.

Figure 2.2: Equivalent circuit for a simple faradaic process.

As in figure 2.1, Rsol and Cdl represent the solution resistance and double layer capacitance, and the new term Rct represents the resistance to charge transfer for the faradaic process. The equivalent circuit shown in Figure 2.2 is generally referred to as the Randels circuit and is most often used as a starting point and then built upon when the initial modeling of an impedance set begins. The Randles circuit is also often used for diffusion controlled, low frequency processes as well and is expanded to include the Warburg impedance as shown in Figure 2.3. The Warburg impedance is encountered whenever diffusion effects completely dominate the electrochemical reaction mechanism and is easily identified by a 45° straight line in impedance plots [82,83].

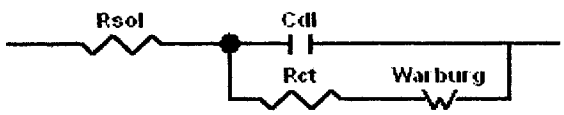

Figure 2.3: Equivalent circuit for a Randles circuit with diffusion control.

It should be noted that to obtain an accurate impedance fit using equivalent circuits, the generated circuit should contain as few circuit elements as possible to

decrease the standard errors of the included parameters and thereby make the applied circuit element valid.

2.5.2. Representation of impedance data

The observed results from EIS experimentation can be expressed in a number of different manners with the most commonly reported in literature being the Nyquist and Bode Plots. The Nyquist plot (also known as Cole-Cole or complex impedance plane plot) is expressed by plotting the imaginary impedance component (Z_{Im}) against the real impedance component (Z_{Re}) for each frequency [83]. As with everything the Nyquist plot has its advantages and disadvantages. Its main advantage is the ease with which the ohmic resistance can be evaluated if data is acquired at high enough frequency and its main disadvantage is that information which is frequency dependant cannot be easily derived from the plot [83]. The other main method of presenting impedance data is the Bode plot. The Bode plot uses the absolute impedance (eq 2.12) and the phase shift ϕ (of the impedance) as a function of the applied frequency. As with the Nyquist plot this method of presenting impedance has its advantages as well. It is easy to see with the Bode plot how impedance is dependant on frequency. Since the logarithm of frequency is plotted this allows for a very wide range of frequency values to be plotted on one graph with each decade given equal weight on the graph. The largest detraction associated with the Bode plot is that the shape of the curve can change if the values for the circuits change. The actual information that can be gathered from impedance information in both the Nyquist and Bode plots will be discussed in greater detail in Section 2.3. Other methods of plotting include Z_{Re} vs. ωZ_{Re} or more commonly known as the Randales plot

which for a simple Randales circuit has the advantage of being a straight line and allows for a more reasonable fit for scattered data points than a Nyquist plot [83]. Also if the polarization resistance is determined, it is then easy to determine the capacitance for the system. Another plotting system that is sometimes encountered involves plotting Y_{Im}/ω vs. Y_{Re}/ω, also known as a capacitance plot. This method is especially useful when circuit elements are in parallel [83]. The capacitance plot allows for easy identification of the capacitance since it only has an imaginary component and subsequently independent of frequency, it shows up as a dot on the graph or requires extrapolation of the line to the y-axis. Comparatively, the resistance has only a real part and its value depends on the frequency which means that it shows up as a straight line on a capacitance plot [83]. Examples of these plotting methods are shown in Figure 5. Although both the Randales and capacitance plots have their uses, they are generally encountered in specific cases including Randales or parallel type circuits and are not listed nearly as often as the Nyquist or Bode plots in the literature.

2.5.3. Experimental applications

If the constant potential case is considered, a small signal perturbation (time dependant) is applied to the equilibrated system to shift it slightly away from its equilibrium position. The applied perturbation must be kept small to ensure that the response of the system to the perturbation remains linear [81]. The applied signal can be a signal wave or a number of waves containing varying amplitudes, frequencies, and phases generated by potential steps, pulse shaped signals or noise [81]. Primarily, signal amplitudes of 10 mV or less are required to maintain linearity of the system especially in

low frequency applications. In high frequency applications the signal can have a higher amplitude since the equivalent circuit can be said to have behavior similar to that in Figure 2.1, and subsequently the bulk of the amplitude signal is consumed by the potential drop of the solution [81]. Normally, there are two techniques for the experimental measurement of impedance: the time domain and frequency techniques [84]. The time domain technique uses a frequency rich signal that acts as a perturbation and the cell response is measured as a function of time. The resulting data is then converted using a transformation algorithm to the frequency domain and the impedance is expressed based on its frequency dependence [84]. The frequency technique uses a sine wave perturbation and the impedance is obtained for a single frequency. This means that numerous measurements over a wide frequency range must be conducted to obtain any useful data and therefore requires a significant amount of time to complete the experiment when compared to the time domain technique [84]. The above information outlines the methods for obtaining impedance data but external input is still required to determine potentials to be studied. This is normally accomplished by examining results obtained from cyclic voltammetry experiments for appropriate areas of interest. These may include, but are not limited by, positive and negative slopes, build up of material on the electrode surface, or gas evolution.

2.5.4. Modeling

The advent of computers has eased the process of modeling an impedance plot to an equivalent circuit diagram significantly. Previously, modeling impedance required a strong background in mathematics and painstaking trial and error were required to develop a reasonable impedance fit with low error values. Currently, there exists several

programs, available commercially, which can model impedance plots quite effectively and only require reasonable starting points. The general method employed in these programs involve the generation of an equivalent circuit, from the elements listed in Table 1, that will hopefully imitate the impedance data set fairly well when values for the parameters are imputed into the program [81]. The second step involves checking the validity of the impedance data using the Kramer-Kronig rule check. This system is derived from the Kramers-Kronig frequency domain transformations. These transformations can allow for the components of one impedance to be calculated from another, the determination of the phase angle from the magnitude of the impedance or the polarization resistance from the imaginary resistance using the equations 2.15-2.19 [81].

$$Z_{Re}(\omega) - Z_{Re}(\infty) = (2\omega/\pi)_0\mu^{\infty} [(xZ_{Im} - \omega Z_{Im}(\omega))/(x^2 - \omega^2)]dx \quad (2.15)$$

$$Z_{Re}(\omega) - Z_{Re}(0) = (2\omega/\pi)_0\mu^{\infty} [((\omega/x)Z_{Im}(x) - \omega Z_{Im}(\omega))/(x^2 - \omega^2)]dx \quad (2.16)$$

$$Z_{Im}(\omega) = -(2\omega/\pi)_0\mu^{\infty} [Z_{Re}(x) - Z_{Re}(\omega))/(x^2 - \omega^2)]dx \quad (2.17)$$

$$\delta(\omega) = -(2\omega/\pi)_0\mu^{\infty} [(\log|Z|)/(x^2 - \omega^2)]dx \quad (2.18)$$

$$\delta(\omega) = (2/\pi)_0\mu^{\infty} [(Z_{Im}(x))/x]dx \quad (2.19)$$

The main condition for the application of the Kramers-Kronig transforms to validating an impedance data set are: the impedance must have finite values for $\omega \rightarrow 0$ and $\omega \rightarrow \infty$, and all intermediate values must be continuous and finite valued functions [81]. The final step employs the use of complex non-linear regression least squares (CNRLS) method of adapting the model parameters to the measured data. In this step both the experimental and the optimized calculated data are plotted and compared (normally using the Nyquist and Bode Plots) to determine how closely the optimized data set compares to the experimental values for the frequency range in question [81]. It

should be noted that although computer simulation has significantly decreased the time required to determine the best fit for a set of impedance values, it is still crucial to start with a reasonable equivalent circuit with the minimal amount of circuit elements to generate a reasonable comparison with the calculated data and maintain low errors to create a valid fit.

Chapter 3

Characterization and Electrochemical Study of Nanoporous Pt Materials

3.1 Introduction

Synthesis of nanomaterials with high surface areas has received significant interest due to their unique properties and a number of impressive applications in catalysis, fuel cells and chemical sensors. Alternative sources of power such as fuel cells have garnered much attention recently due to their efficiency and non harmful impact on the environment. A self supported substrate for direct immobilization of Pt nanoparticles and Pt 3D nanoporous networks is desirable for large surface areas and high performance electrodes.

3.2 Characterization of Nanoporous Pt Electrodes

The surface morphologies of the Ti substrate and nanoporous platinum networks developed in this study were analyzed by Scanning Electron Microscopy (SEM). Figure 3.1 represents a blank Ti substrate (a: sample S1) and electrochemical deposition with chloroplatinic acid and hydrochloric acid for 3 minutes at -10 mA (c: sample S2), 2 minutes at -20 mA (e: sample S3) and 3 minutes at -20 mA (g: sample S4). As shown in these images, there is a consistent coverage of particles on the surface of the electrodes. The amount of dispersed platinum particles increases as electrochemical deposition time and current are increased. Figures 3.1.b,d,f,h illustrate the effect of hydrothermal treatment using the aforementioned acid solution and ethylene glycol at 100°C for 10 hours. This resulted in the formation of a nanoporous platinum network. It can be seen that the size and coverage of network is increased as the effect of electrochemical

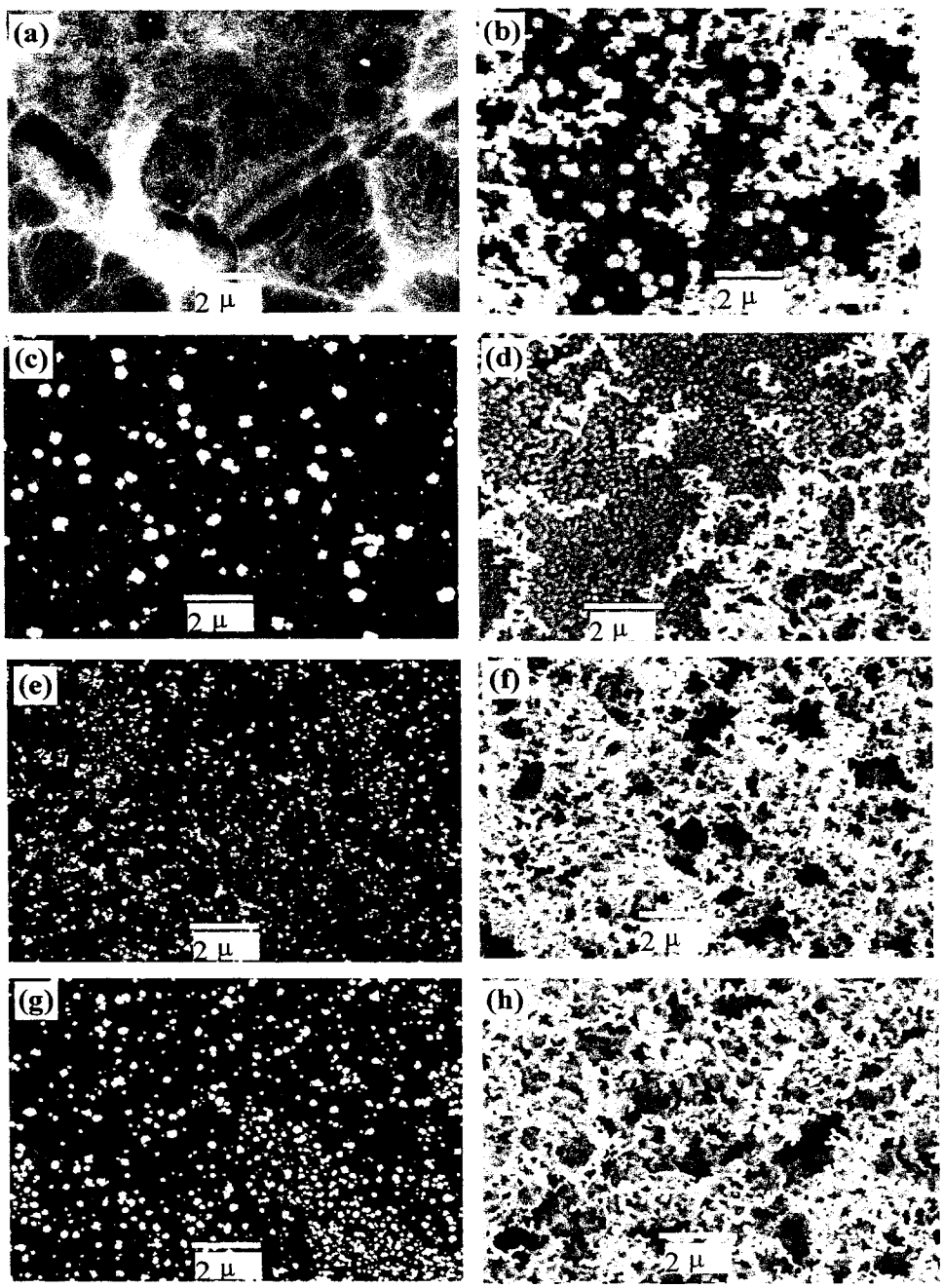

Figure 3.1. SEM Images: electrochemical deposition / hydrothermal treatment (100°C, EG, 10 hours): (a) and (b) blank Ti substrate, (c) and (d) at -10 mA for 3 min, (e) and (f) at -20 mA for 2 min, (g) and (h) at -20 mA for 3 min.

deposition is greatened. Sample S1 shows the formation of a small network, while S4 displays a large network completely covering the electrode surface. Further XRD analysis provided support for the formation of the nanoporous platinum network. Figure 3.2 shows the XRD results of S4 after (a) electrochemical deposition and (b) hydrothermal treatment. The pattern in (b) shows that there is a sharp increase in the amount of platinum present prior to heating. The above SEM images show that the nanoporous platinum network electrodes developed in this work possess a much larger surface area compared to a bulk platinum electrode which is important for industrial electrochemical applications.

Figure 3.3 shows the temperature effect on the growth of the nanoporous platinum network on a Ti substrate. In Figure 3.3.a (75°C), there is little formation of the platinum network. Increasing the temperature slightly, Figure 3.3.b (100°C), shows small networks of platinum. When comparing this blank sample with the blank sample represented in Figure 3.1.b, it can be seen that the increased concentration of the electrochemical deposition/hydrothermal solution (2 times) increases the formation of the platinum network. At elevated temperatures of 150°C and 180°C, Figures 3.3.c-d, large platinum networks are formed with near complete coverage of the electrode surface.

3.3 Hydrogen Adsorption and CO Oxidation

Cyclic voltammetry was used to characterize the nanoporous platinum electrodes in a 0.5 M H_2SO_4 solution. Part a of Figure 3.4 shows CV curves for sample S1 (dashed, blank), S2 (dotted, at -10 mA for 3min), S3 (dash dot dash, at -20 mA for

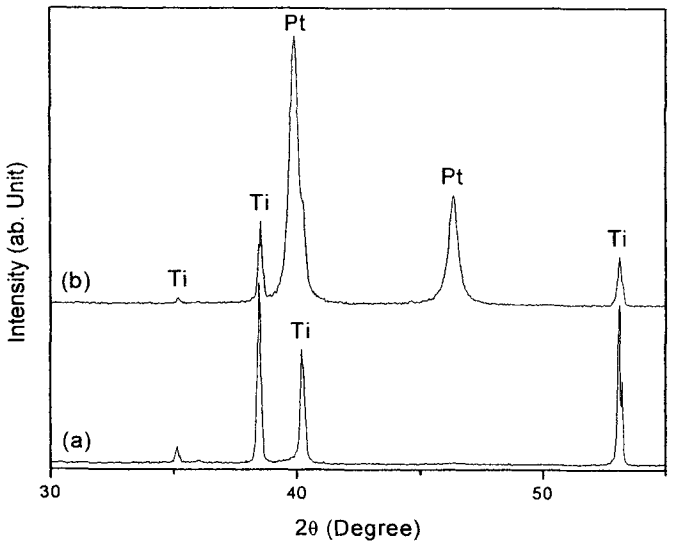

Figure 3.2. XRD patterns of (a) a nanoporous Pt network electrode and (b) blank Ti Substrate.

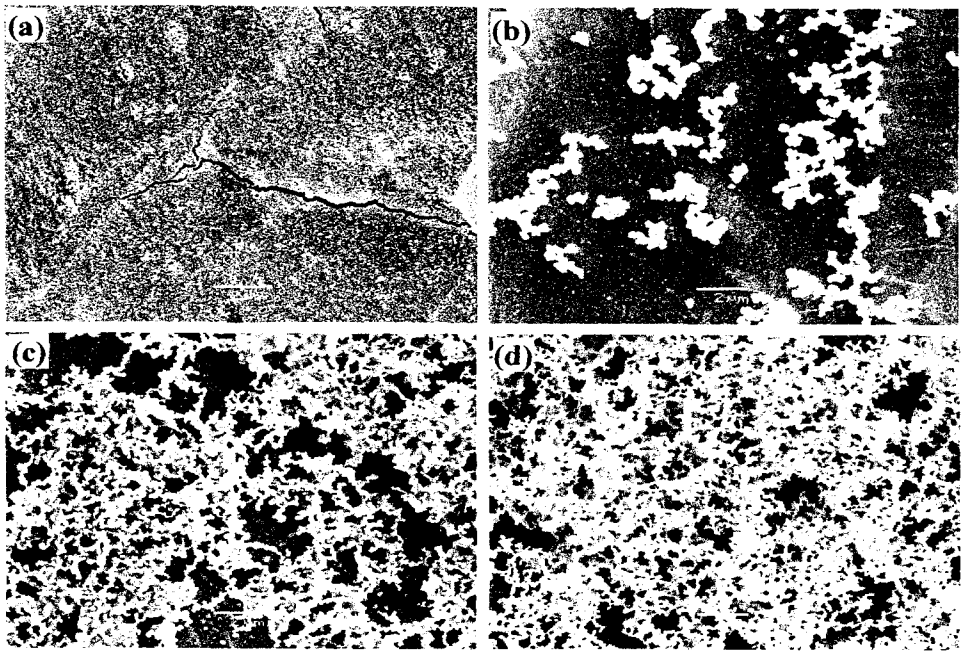

Figure 3.3. SEM Images of temperature effect: (a) 75°C, (b) 100°C, (c) 150°C and (d) 180°C with the Ti substrates covered by electrodeposition of Pt (-20 mA/cm^2, 60 seconds, H_2PtCl_6, HCl)

2min), S4 (dash dot dot dash, at -20 mA for 3min) at a potential sweep rate of 20 mV/s. All four samples have consistent hydrogen adsorption/desorption behavior: two reversible peaks at approximately -0.16 V and -0.019 V. For each sample, the peak at -0.019 V is weaker than the peak at -0.16 V. The intensity of the peaks varies for the four curves and the integrated intensity of the peaks is an approximation of the number of Pt sites available for hydrogen adsorption/desorption. In calculating the hydrogen adsorption charge on electrode surfaces, an assumption is made that the double layer charging is constant over the whole potential range. The charge of S1 is 0.83 $mC.cm^{-2}$ which is about 4 times larger then what has been reported for polycrystalline Pt (0.21 $mC.cm^{-2}$) [85]. S4 has a charge of 4.13 $mC.cm^{-2}$, 20 times larger then Pt wire. This means that the actual surface of the nanoporous platinum electrodes is much greater then polycrystalline Pt. S4 had the highest intensity, followed by S3, S2 and S1. This is in good agreement with the displacement of the networks as seen in Figures 3.1.b,d,f,h. These CV curves exhibit similar features to those previously reported for polycrystalline Pt electrodes [85,86].

The adsorption and oxidation of CO was studied. This is important because the ability of the catalyst to effectively oxidize CO is a primary issue with DMFCs [87-89]. CV's of the four electrodes were conducted in 0.5 M H_2SO_4. Just prior to scanning with cyclic voltammetry, the potential of the electrodes was held at -0.1 V for 450 seconds. Initially the solution was purged with CO for 90 seconds, and then with Ar for the remaining pre-treatment time. Figure 3.4.b shows the first cycle and second forward cycle for S1, S2, S3 and S4. During the first forward cycle, hydrogen adsorption is

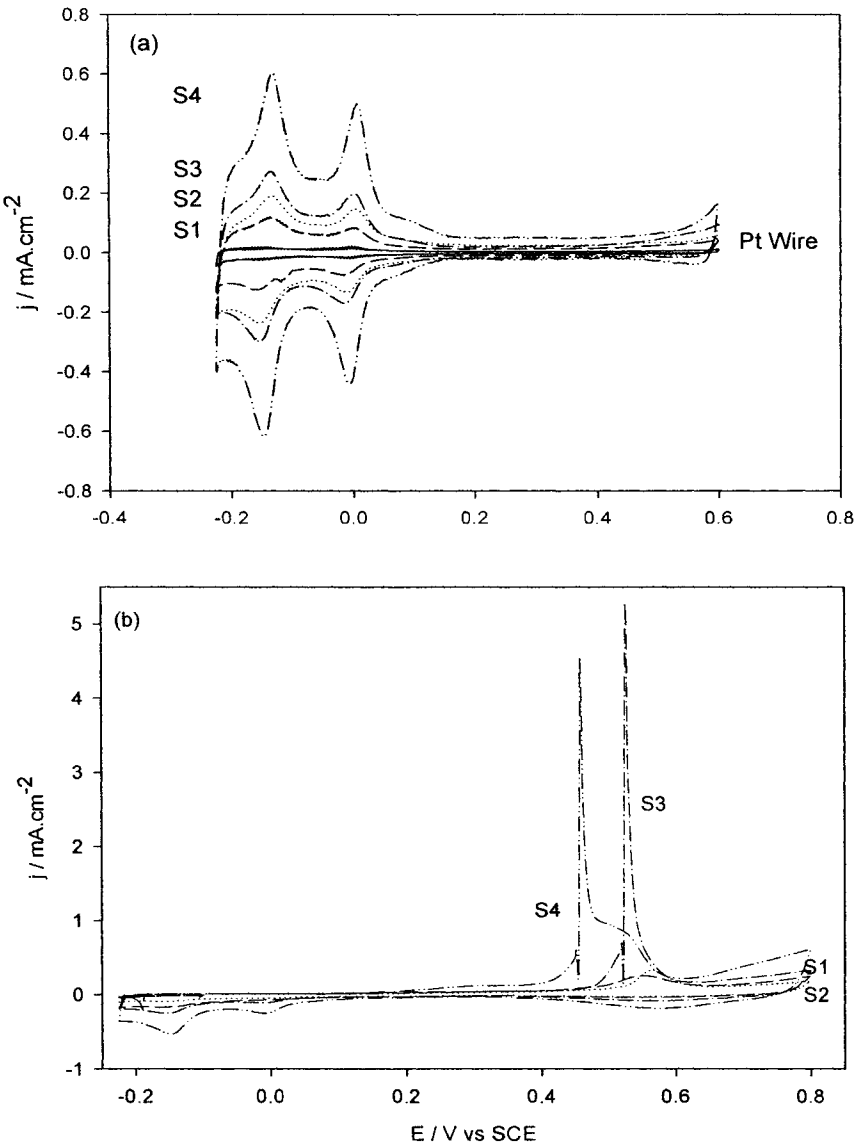

Figure 3.4. Cyclic voltammograms of (a) S1, S2, S3, S4 and Pt Wire and (b) initial cycle of CO oxidation scan in 0.5 M H_2SO_4 at a potential scan rate of 20 mV/s.

Table 3.1: Values of Q_{CO} and Q_H obtained from the cyclic voltammegrams in 0.5 M H_2SO_4 purged with CO.

Electrode	Q_{CO} (mC/cm^2)	Q_H (mC/cm^2)	Q_{CO}/Q_H
S1	1.30	0.83	1.57
S2	1.65	1.29	1.28
S3	4.30	2.16	1.99
S4	6.95	4.13	1.68

minimized, signifying that the active sites of platinum on the nanoporous network electrodes are covered by adsorbed CO. On each of the samples there are two CO oxidation peaks: one large peak at approximately 0.45 V with a small shoulder at 0.5 V. The second scan contains hydrogen adsorption/desorption peaks, but no CO peaks. This means that the CO is completely oxidized on the first forward scan. Table 3.1 lists the charges associated with CO oxidation (Q_{CO}) and hydrogen desorption (Q_H). There is a proportion between the Q_{CO} and Q_H for the individual electrodes. The ratio of Q_{CO}/Q_H varies from 1.28 to 1.99 which suggests that the carbon monoxide is both linearly and non-linearly bound to the nanoporous platinum network. All of the electrodes exhibited similar features on the curves; however, the intensity of the peaks and onset of CO oxidation was different. Samples S1, S2, S3 and S4 showed similar intensity patterns to those seen in Figure 3.2.a. CO oxidation for S1-S3 started at 0.2 V while S4's onset of oxidation was shifted slightly lower to 0.15 V. The oxidation potentials for these 4 samples are lower than those observed for bulk Pt (0.4 V). These results indicate that the effect of the nanoporous platinum network increases catalytic activity towards to oxidation of CO.

3.4 Methanol Oxidation and Chronoamperometry

Another important factor in DMFC is the activity of the catalyst towards methanol oxidation. Cyclic voltammetry studies were conducted in a 0.1 M CH_3OH + 0.5 M H_2SO_4 solution at a potential sweep rate of 20 mV/s. In order to obtain a direct comparison to bulk platinum, a platinum wire electrode was included in these experiments. Figure 3.5.a shows short range CV scans, between -0.225 V and 0.8 V, for each of the electrodes. As

is seen from the graphs, the nanoporous platinum network electrodes show a much greater tendency towards methanol oxidation then the platinum wire. Samples S1, S2, S3, and S4 all show higher current densities, broader peaks, and a lower onset of methanol electro-oxidation than the polycrystalline platinum. S4, in particular, containing a large surface area, indicates an activity towards methanol oxidation of over 20 times that of bulk platinum as seen in Figure 3.5.a. The platinum wire shows the start of methanol electro-oxidation at 0.4 V. S1-S3 have their oxidation of methanol beginning at 0.3 V, while S4's onset of oxidation is even lower at 0.15 V. These lower potential are significant because methanol can break-down spontaneously on Pt electrodes to form CO and other inhibiting species which cover the active sites of the Pt surface and prevent the electro-oxidation of methanol at potentials lower then 0.4 V. The ability of the nanoporous platinum network electrodes to lower the onset of methanol oxidation of 0.4 V (Pt wire) to as low as 0.15 V (S4) means that they are more efficient at removing species that may stop the catalyst from oxidizing methanol.

Further experiments were conducted to test the electrodes ability towards methanol electro-oxidation by way of chronoamperometry. In these potentiostatic studies, the potential was held at an initial value j_1, and then stepped up to a final potential j_2 and held there for t seconds. A potential of j_1 = 0 V was applied for 30 seconds and then stepped up to j_2 = 0.6 V and held there for 300 seconds. Figure 3.5.b shows five potentiostatic curves, including that of a platinum wire for comparison. At j_2 = 0.6 V, in between the minimum and maximum current densities for methanol electro-oxidation, the differences in steady state current are readily observed. At t = 300 seconds, the steady

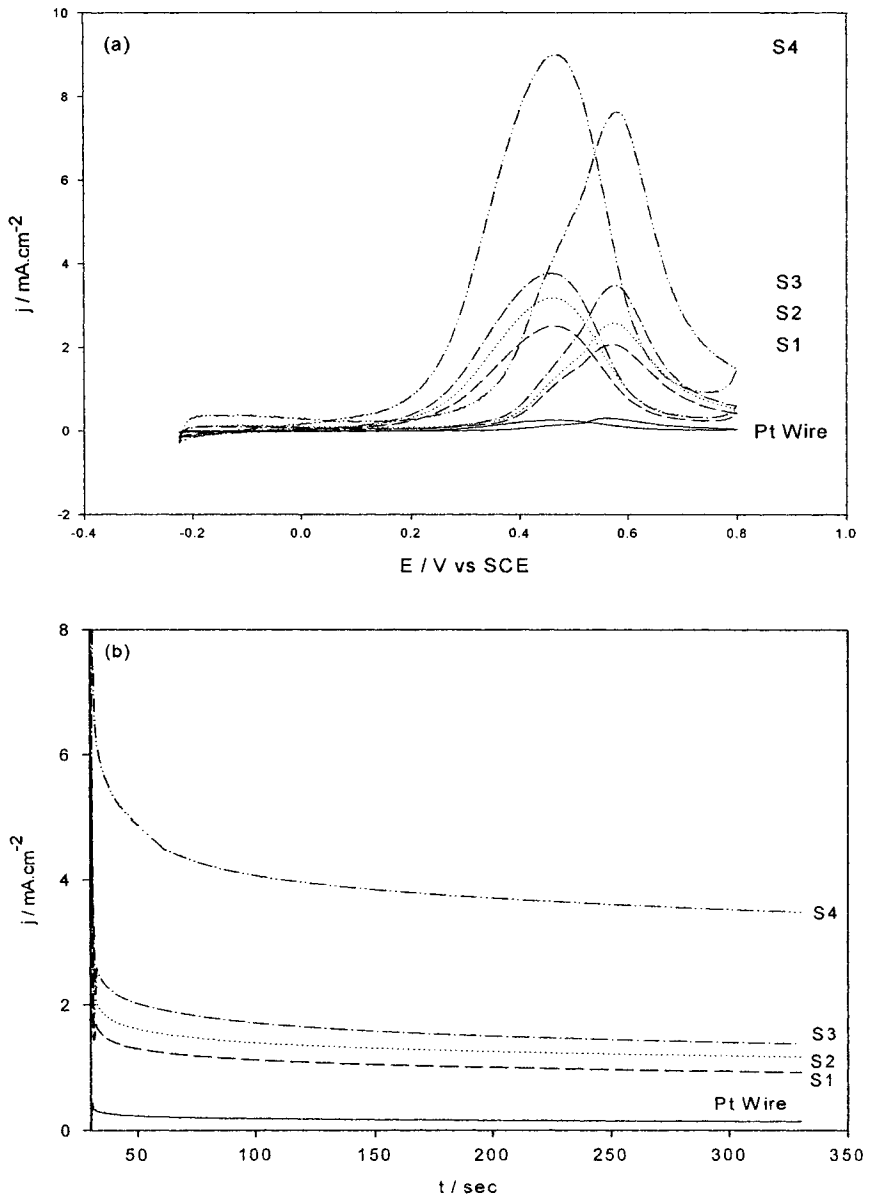

Figure 3.5. Cyclic Voltammograms of (a) S1, S2, S3, S4 and Pt Wire in a solution of 0.5 M H_2SO_4 + 0.1 M CH_3OH at a potential scan rate of 20 mV/s and (b) chronoamperometry at a potential of 600 mV.

state current is over 25 times that of the Pt wire. These studies fit well with the CVs in Figure 3.5.a, and are consistent with the performance of the electrodes as shown in Figure 3.4.a. All of these results show that the activity of these electrodes towards methanol oxidation is more enhanced then that of bulk platinum.

3.5 Electrochemical Impedance Study

To further investigate the performance of these electrodes, electrochemical impedance spectroscopy was utilized in a 0.1 M CH_3OH + 0.5 M H_2SO_4 solution. This serves as another method of studying the activity of these nanoporous platinum network electrodes towards the oxidation of methanol. Figure 3.6.a presents a Nyquist plot at an electrode potential of 300 mV, where Z_i and Z_r are the imaginary and real components of the impedance. The frequency was changed from 40 kHz to 25 mHz. S1 can be seen to have significantly lower impedance on both the imaginary and real axes, when compared to the Pt wire. Due to their small impedance relative to the Pt wire, samples S1-S4 are presented as an inset to Figure 3.6.a. The impedance becomes progressively smaller going from S1 to S2 to S3 to S4. For a better understanding of the impedance results, an equivalent electric circuit was used to fit the experimental data, with the impedance results being represented by symbols and the fit data by lines.

Figure 3.6.b shows the equivalent circuit used to fit the data in Figure 3.6.a. This is a parallel $R_s(R_{ct}CPE)$ circuit where R_s represents the uncompensated solution resistance, while the parallel combination of the charge transfer resistance (R_{ct}) and the constant phase element (CPE) take into account the methanol adsorption and oxidation. The parallel combination ($R_{ct}CPE$) leads to a depressed semi-circle in the corresponding

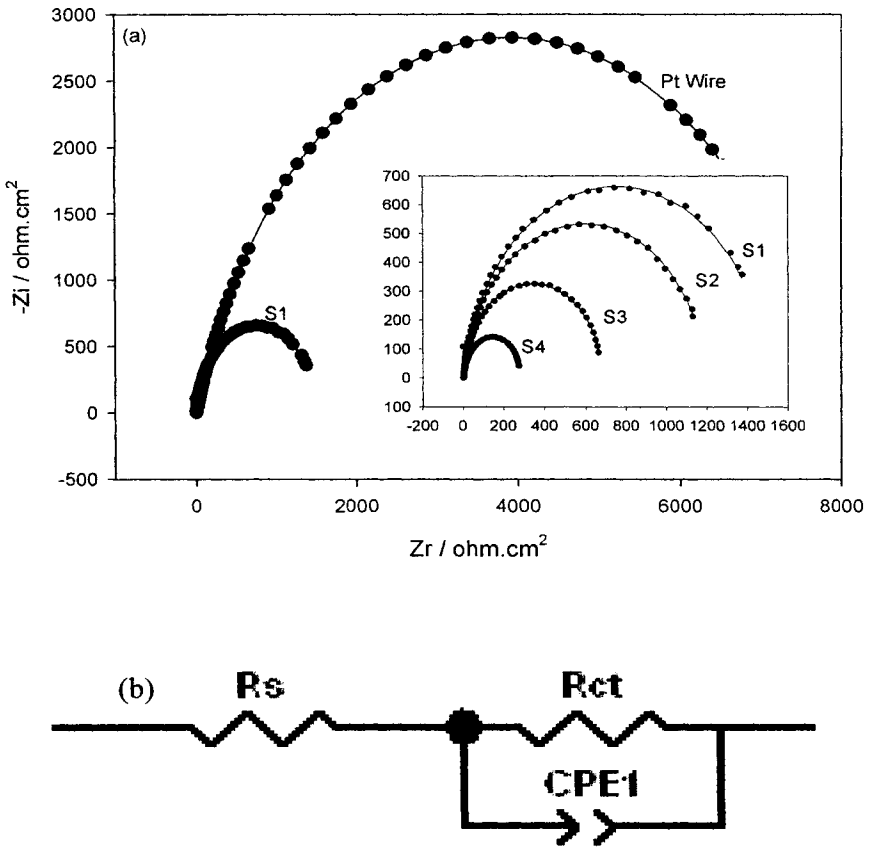

Figure 3.6. Electrochemical Impedance Spectra of (a) S1, S2, S3, S4 and Pt Wire in a 0.5 M H_2SO_4 + 0.1 M CH_3OH solution at a potential of 300 mV and (b) the equivalent circuit used to fit the impedance data.

Table 3.2: Impedance Components for Positive Faradaic Impedance on S1, S2, S3, S4, and S5 by Fitting the Experimental Data Measured in a 0.5 M H_2SO_4 + 0.1 M CH_3OH Solution Using the Equivalent Circuit Shown in Figure 3.5e.

		R_{ct} (Ω cm^2)		CPE-T (mF cm^{-2})		CPE-P	
Potential	**Electrode**	**Value**	**Error%**	**Value**	**Error%**	**Value**	**Error%**
300 mV	Pt wire	7178	3.15	0.14	2.49	0.83	0.46
	S1	1525	5.88	0.57	4.15	0.93	1.07
	S2	1200	5.12	0.63	4.37	0.91	1.00
	S3	685	6.52	0.87	4.85	0.96	1.04
	S4	275	5.77	1.83	5.29	0.95	1.42

Nyquist impedance plot. The CPE is defined by CPE-T and CPE-P. If CPE-P equals 1, then the CPE is considered a capacitor C_{dl}. Table 3.2 summarizes all of the values for the parameters R_{ct}, CPE-T, CPE-P and their associated error computed by the fitting of the experimental EIS data. All the associated errors are within 7 %, meaning that the proposed model shown in Figure 3.6.b fits the experimental data effectively. The CPE-T value for S1 is larger then the value for the Pt wire, S2 is greater then S1, S3 is larger then S2, and S4 has the greatest value. All electrodes showed a CPE-P result of approximately 0.9 which means the CPE-T values are close to the C_{dl}. Charge transfer resistance value decreased, in turn, going from the Pt wire (7178 Ω) to sample S4 (275 Ω). These results are in good agreement with the double-layer charging that was seen in Figure 3.4.a.

3.6 Summary

The fabrication and performance of nanoporous platinum network electrodes has been investigated by a variety of methods such as Scanning Electron Microscopy (SEM), Cyclic Voltammetry (CV), Chronoamperometry (CA), and Electrochemical Impedance Spectroscopy (EIS). SEM images show that increasing exposure of the substrate to electrochemical deposition, combined with hydrothermal treatment, has the effect of increasing the displacement and surface area of the nanoporous platinum network. Samples S1-S4 all show substantial increases in activity and surface area when compared to Pt wire. S4 has an active surface area of greater then 20 times that of Pt wire, due to the large displacement of the nanoporous platinum network. CO oxidation occurs at low electrode potentials. The activity of the electrodes towards methanol electro-oxidation

was also studied, with the results showing that the four samples, S1-S4, all lower the onset of methanol electro-oxidation when compared to polycrystalline platinum. Sample S4 lowered the start of oxidation from 0.4 V (Pt wire) to 0.15 V. Chronoamperiometry experiments indicate that the steady state current of t = 300 seconds for S4 is 25 times greater than that of bulk platinum. Charge transfer resistance in EIS studies for the nanoporous samples was much lower than that for the Pt wire. In conclusion, the results presented have shown that the nanoporous platinum electrodes have a much larger surface area and higher activity than the bulk platinum. Their activity towards methanol oxidation is enhanced. They are much more efficient catalysts than their polycrystalline counterparts.

Chapter 4

Effect of Ruthenium on the Electrocatalytic Performance of Nanoporous Platinum Materials Towards Methanol Oxidation and Non-Enzymatic Glucose Sensing

4.1 Introduction

In an effort to further enhance the activity of the 3D Pt network electrodes, a co-catalyst, ruthenium, was added as bimetallic platinum-ruthenium has been shown to exhibit the best activity towards methanol oxidation [21-24]. In this study ruthenium nanoparticles were uniformly dispersed into 3D structures by way of a hydrothermal precipitating process from a Ru colloid solution composed of $RuCl_3$, citric acid, and $NaBH_4$. This resulted in the formation of the 3D nanoporous PtRu network electrodes.

4.2 Characterization and Analysis of Ruthenium Enriched Nanoporous Electrodes

The SEM images of the surface morphologies of the prepared electrodes with different ratios of Ru are shown in Figure 4.1. Nanoporous Pt networks were formed as shown in Figure 4.1.a. Figure 4.1.b-e show the SEM images of the samples with 5%, 19%, 41% and 59% Ru, respectively. The surface structures look similar to that of nanoporous Pt, even with the Ru concentration up to 59%; but the diameters of the particles were increased slightly with the increasing ratio of Ru. With the Ru ratio up to 59%, Figure 4.1.e shows that partial porous structures were covered by Ru nanoparticles, which means that some pores were filled by Ru nanoparticles. These results indicate that the porous structure is suitable for Ru nanoparticle loading with a ratio of Ru up to 41% on the surface of 3D Pt networks without local precipitation or damage to the nanoporous

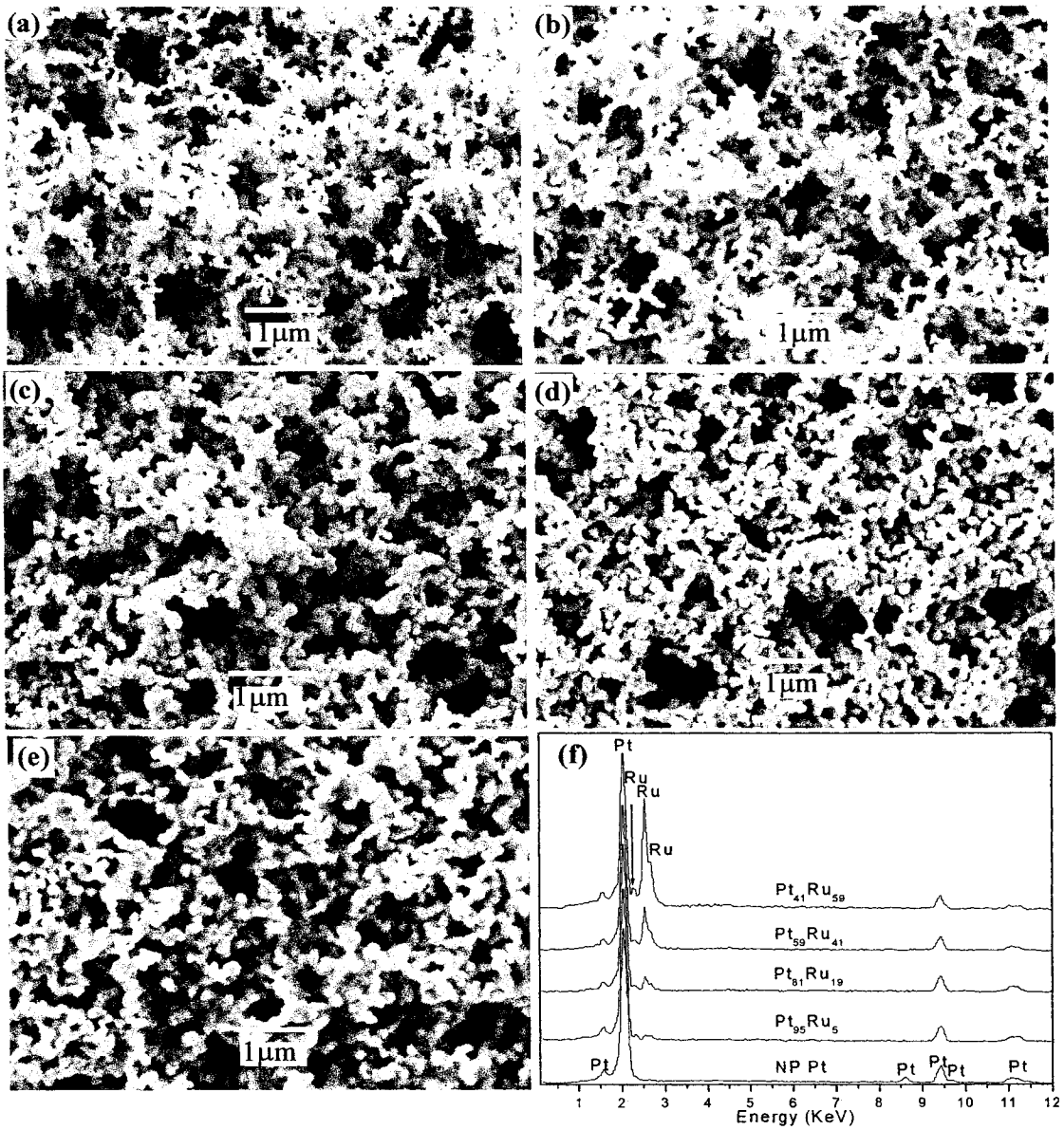

Figure 4.1. SEM images of (a) nanoporous Pt; (b) nanoporous $Pt_{95}Ru_5$; (c) nanoporous $Pt_{81}Ru_{19}$; (d) nanoporous $Pt_{59}Ru_{41}$, (e) nanoporous $Pt_{41}Ru_{59}$; and (f) their EDS spectra.

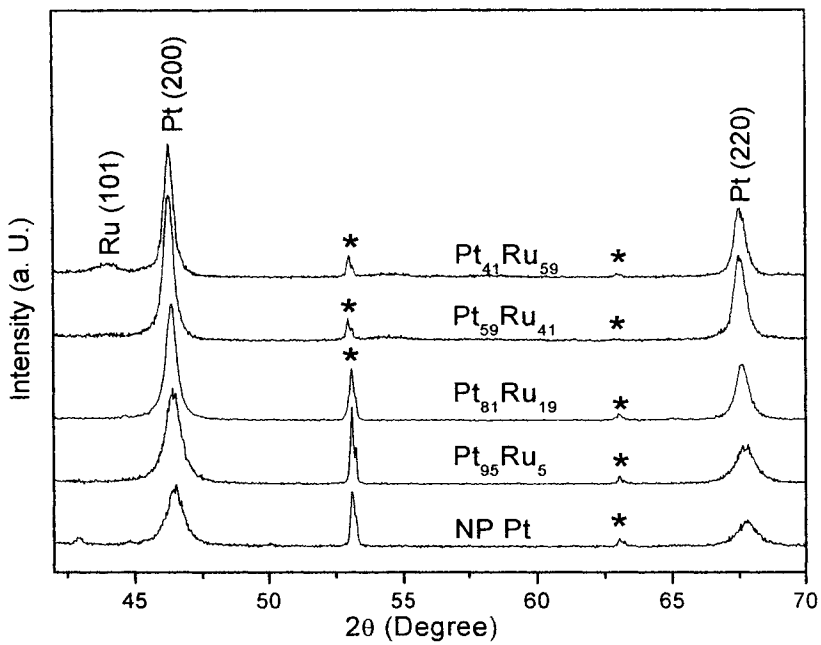

Figure 4.2. XRD patterns of the nonporous Pt and Pt-Ru electrodes used for this study. The * denotes Ti.

structure. The corresponding EDS spectra from down to up are displayed in Figure 4.1.a-e, respectively. These results show that the Ru atomic ratios of the samples as shown in Figure 1a to 1e are 0%, 5%, 19%, 41% and 59%, respectively.

The XRD patterns of the as-synthesized electrodes are shown in Figure 4.2. The peaks marked by an asterisk are derived from the titanium substrate. All the remaining peaks of nanoporous (NP) Pt, and NP PtRu up to 41%, are consistent with the face-center-cubic (fcc) pattern expected for Pt-rich Pt-Ru alloys [90]. Peaks associated with this alloy phase are identified by the appropriate Miller indices as shown in the patterns. These results indicate that there is no crystalline metal phase separation that might have occurred during synthesis as a Ru peak is not observed for the samples with a Ru atomic ratio up to 41%. However, when the Ru concentration is 59%, a diffraction peak near 44° in 2θ from Ru metal is observed which means crystalline metal phase separation has taken place.

4.3 Ruthenium Influence on Hydrogen Adsorption and CO Oxidation

The details of the effect of Ru doping were further studied by changing the Ru concentration in the PtRu electrodes. Figure 4.3.a shows the CV of the NP Pt electrodes with 5%, 19%, 41% and 59% in 0.5 M H_2SO_4 at a potential scan rate of 20 mV/s. As the amount of Ru increases, the hydrogen adsorption/desorption region begins to lose structure and an increase of the charge in the double-layer region is also observed. This increase in the double-layer region has been previously described and it has been used to estimate the amount of Ru for platinum single crystals decorated by spontaneous deposition with Ru. As noticed by Gasteiger et al. [91] it indicates the formation of

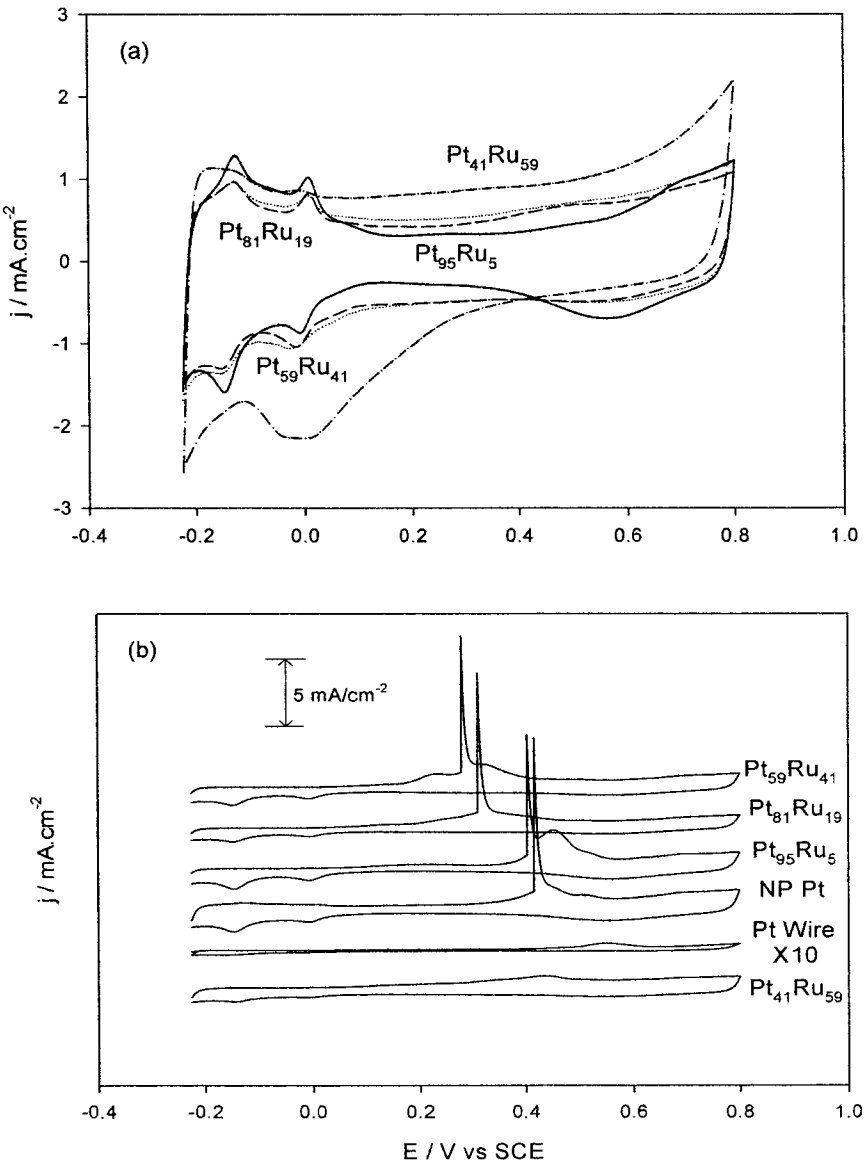

Figure 4.3. (a) Cyclic voltammograms of NP Pt, NP $Pt_{95}Ru_5$, NP $Pt_{81}Ru_{19}$, NP $Pt_{59}Ru_{41}$, NP $Pt_{41}Ru_{19}$ and Pt Wire; and (b) initial cycle of CO oxidation scan. Solution: 0.5 M H_2SO_4; Potential scan rate: 20 mV/s.

oxygen-like species on the surface at more negative potentials. This plays an important role in progressively lowering the potential of irreversible CO electrooxidation. CO adsorption-oxidation may be quantitatively used as a composition and structure sensitive surface probe [92]. The stripping peak of CO on the NP Pt electrode is at a slightly lower potential than that on the polycrystalline Pt as seen in Figure 4.3.b. Moreover, the slight modification of the NP Pt electrode with Ru 5.1% brought a significant change in the CO stripping peak. The further doping (Ru 19% and 41%) of NP Pt lowers the CO stripping peaks down to 0.32 for 19% Ru and 0.28 V for 41% Ru. However, increasing the Ru concentration up to 59% shows increased CO stripping peak potential around 0.44 V. It was reported by Gasteiger et al. that the maximum activity toward CO oxidation could be achieved by a Ru surface composition of 50%, since it maximizes the number of Pt-Ru neighbors and hence provides more nucleation sites [93]. The CO oxidation on Pt/Ru nanoparticles shows very similar trends to those on poly/single crystalline Pt/Ru alloy surfaces. In both cases, Ru sites near Pt atoms nucleate oxygen-containing species ($-OH_{ads}$) at low electrode potentials and, thereby, lower the onset potential of CO oxidation.

4.4 Electrocatalytic Properties of Ruthenium During Methanol Oxidation

There is wide acceptance that PtRu is the most promising electrocatalyst for methanol oxidation [21-24]. Methanol oxidation CV's for NP Pt electrodes doped with different Ru concentrations are shown in Figure 4.4.a (forward scan) and Figure 4.4.b (backward scan) in 0.5 M H_2SO_4 + 0.1 M CH_3OH at a potential scan rate of 20 mV/s. In the previous chapter, we discussed that the methanol oxidation performance of NP Pt

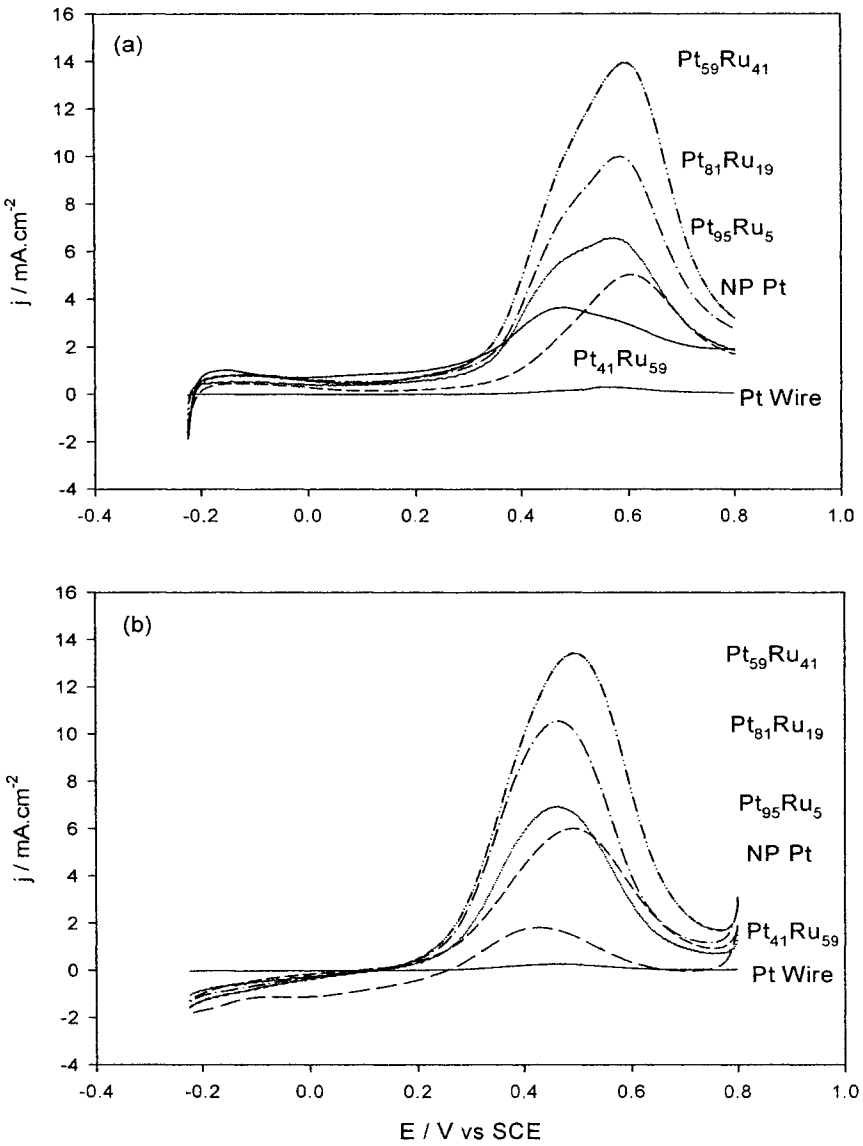

Figure 4.4. (a) Forward cyclic voltammograms of NP Pt, NP $Pt_{95}Ru_5$, NP $Pt_{81}Ru_{19}$, NP $Pt_{59}Ru_{41}$, NP $Pt_{41}Ru_{19}$ and Pt Wire; and (b) the reverse scan. Solution: 0.5 M H_2SO_4; Potential scan rate: 20 mV/s.

network electrodes was significantly larger than that on PC Pt. When the methanol oxidation on NP Pt is compared with the oxidation on NP Pt doped with different amounts of Ru, some important features should be noted. The oxidation current increases from NP Pt to NP PtRu-41%, and then falls down to NP PtRu-59%. This delay seems due to the presence of higher amounts of Ru on the surface, which is inert for the methanol dehydrogenation. However, the onset of the methanol oxidation shifts to lower potentials than for pure Pt. These results show that NP Pt/Ru-41% exhibits better methanol oxidation activities than the other electrodes, as higher methanol oxidation currents are observed at relatively lower potentials. It is known that another method to benchmark the catalyst performance is to compare the ratio of current densities associated with the anodic peaks in the forward (j_f) and reverse (j_b) scans. Such a ratio has been used to infer the CO tolerance of the catalysts [88]. A lower j_f/j_b value signifies poor oxidation of methanol to CO_2 during the anodic scan and excessive accumulation of carbonaceous species on the catalyst surface, namely, a greater extent of CO poisoning. Hence a higher j_f/j_b value is indicative of improved CO tolerance. When comparing the corresponding j_f/j_b values of the samples calculated from Figure 4.4.a-b, it can be clearly seen these values increase with the increasing Ru composition with the NP Pt electrodes. Considering both the oxidation current density and the j_f/j_b value, in this case, the NP Pt electrode with Ru 41% shows the best performance for oxidation of methanol.

4.5 Further Development of the Fabrication of Nanostructured Pt-Ru Materials

Thus far, the production of bimetallic nanostructured Pt-based materials required several steps to fabricate the electrode. These include electrochemical deposition, two

hydrothermal treatment steps, several rinsing/drying cycles and the use of numerous chemicals. We sought to produce a method where nanostructured PtRu electrodes could be made in a single step. A solution of H_2PtCl_6, $RuCl_3$, CH_2O and HCl was placed inside a Teflon® lined autoclave with Ti substrates and then subjected to a single hydrothermal treatment. The result was the formation of high performance nanostructured PtRu material electrodes.

4.6 Characterization of High Performance PtRu Electrodes

SEM was used to characterize the surface morphologies of 3D nanoporous PtRu alloy network electrodes after hydrothermal treatment. Figures 4.5.a-d show SEM images containing good coverage of the substrate for samples of nanoporous Pt (S5), Pt/Ru-12% (S6), NP Pt/Ru-38% (S7) and NP Pt/Ru-56% (S8) respectively. The increase in diameter of the porous networks can be readily observed as the ruthenium concentration increases, with a range in size from 10's to 100's of nanometers. Further analysis of the sample was done by energy dispersive X-ray spectrometry and X-ray diffraction. Asterisks in Figure 4.5.e and Figure 4.5.f denote the presence of titanium. The EDS spectra shown in Figure 4.5.e indicate the increase in ruthenium concentration from S5 to S8. XRD patterns in Figure 4.5.f indicate peaks consistent with the face-center-cubic (fcc) pattern anticipated for platinum rich PtRu alloys [90]. A decrease in platinum concentration as ruthenium concentration increases is observed; however, no diffraction peak for ruthenium is observed which would suggest that a PtRu alloy has been formed on the surface of the sample. Based on the SEM images, we propose a growth method similar to the seed process previously reported. At appropriate temperature and pressure,

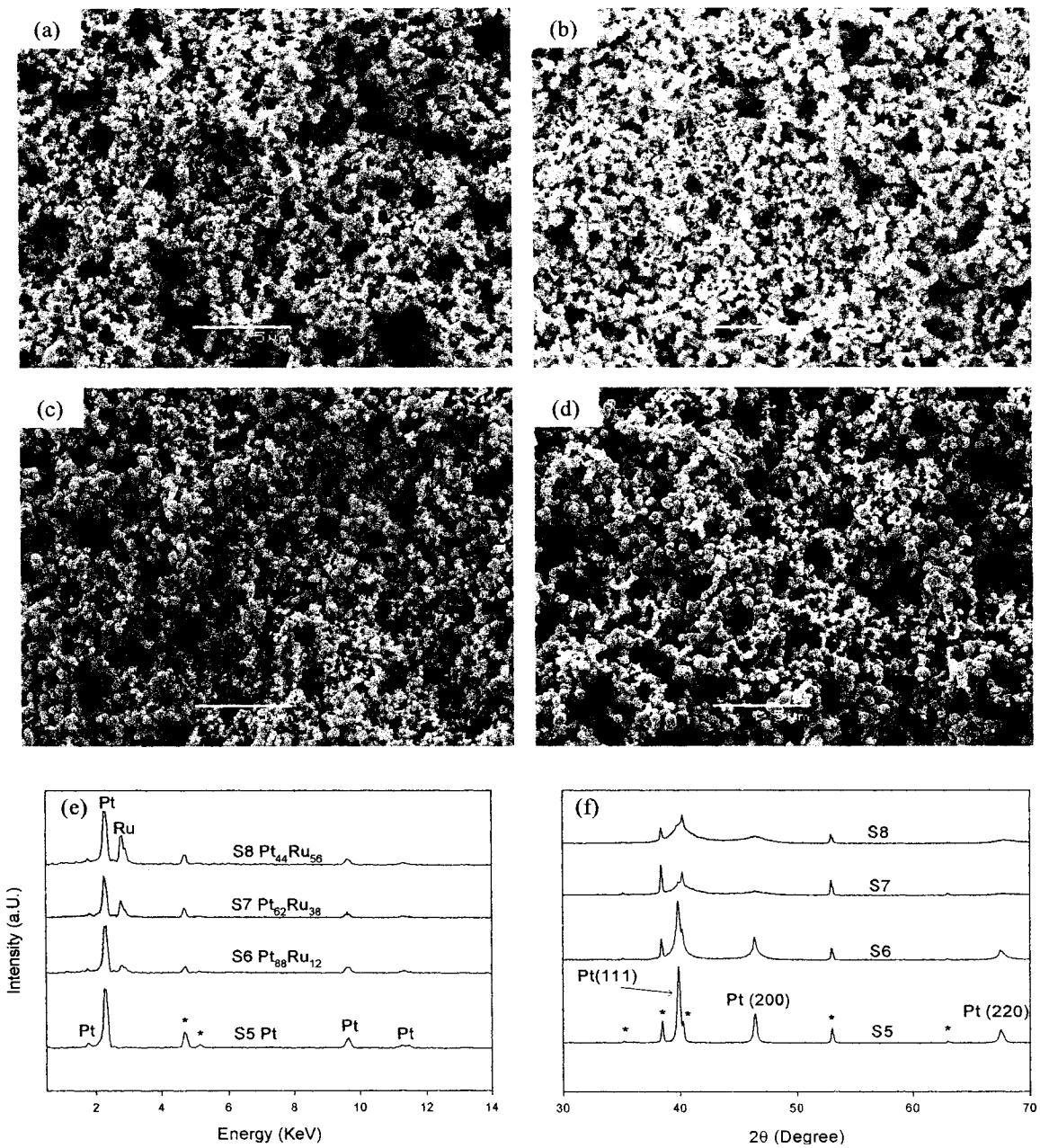

Figure 4.5. SEM Images: (a) Nanoporous Pt (S5); (b) Nanoporous Pt/Ru-12% (S6); (c) Nanoporous Pt/Ru-38% (S7); (d) Nanoporous Pt/Ru-56% (S8). The corresponding EDS spectra (e) and XRD patterns (f) of the samples shown in (a) to (d) .

the formaldehyde reduces the platinum from Pt^{4+} to Pt^0 and ruthenium from Ru^{3+} to Ru^0 resulting in deposition on the titanium substrate surface. As reduction continues, the surface of the substrate gets covered until the nanoparticles start forming on top of one another culminating in the formation of the 3D NP PtRu alloy network.

4.7 Electrocatalytic Activity of the High Performance PtRu Electrodes

Electrochemical studies were used to evaluate the electrochemical properties of the 3D alloy electrodes. The adsorption and desorption of hydrogen is a powerful technique in determining the active surface area of a platinum electrode [94]. As the ruthenium concentration of the electrodes increased, the double layer capacitance increased while the structure of the hydrogen region became less defined. These observations are consistent with those of Wieckowski's group [92]. Figure 4.6.a shows a short range CV scan for S5, S6, S7, S8 and S9 (Pt Wire) in a 0.5 M H_2SO_4 solution at a potential scan rate of 20 mV/s. The hydrogen adsorption/desorption peaks for each sample are consistent with a slight shift from polycrystalline Pt (ca. 0.00025 V, -0.14V) to S4 (ca. -0.026 V, -0.17V). The actual surface area of the electrodes is equivalent to the number of Pt sites available for hydrogen adsorption/desorption. In calculating the adsorption charge, integrated area under the peaks, we assume that the double layer capacitance is constant across the entire potential range. The hydrogen adsorption charge (Q_H) of polycrystalline Pt was calculated at 0.21 mC/cm^2. Samples S5, S6, S7, & S8 produced Q_H's of 4.85, 16.01, 28.48, and 30.23 mC/cm^2, respectively. These results show that the surface area of these samples is many times that of polycrystalline Pt, especially S7 and S8 whose actual surface areas are well in excess of 100 times greater.

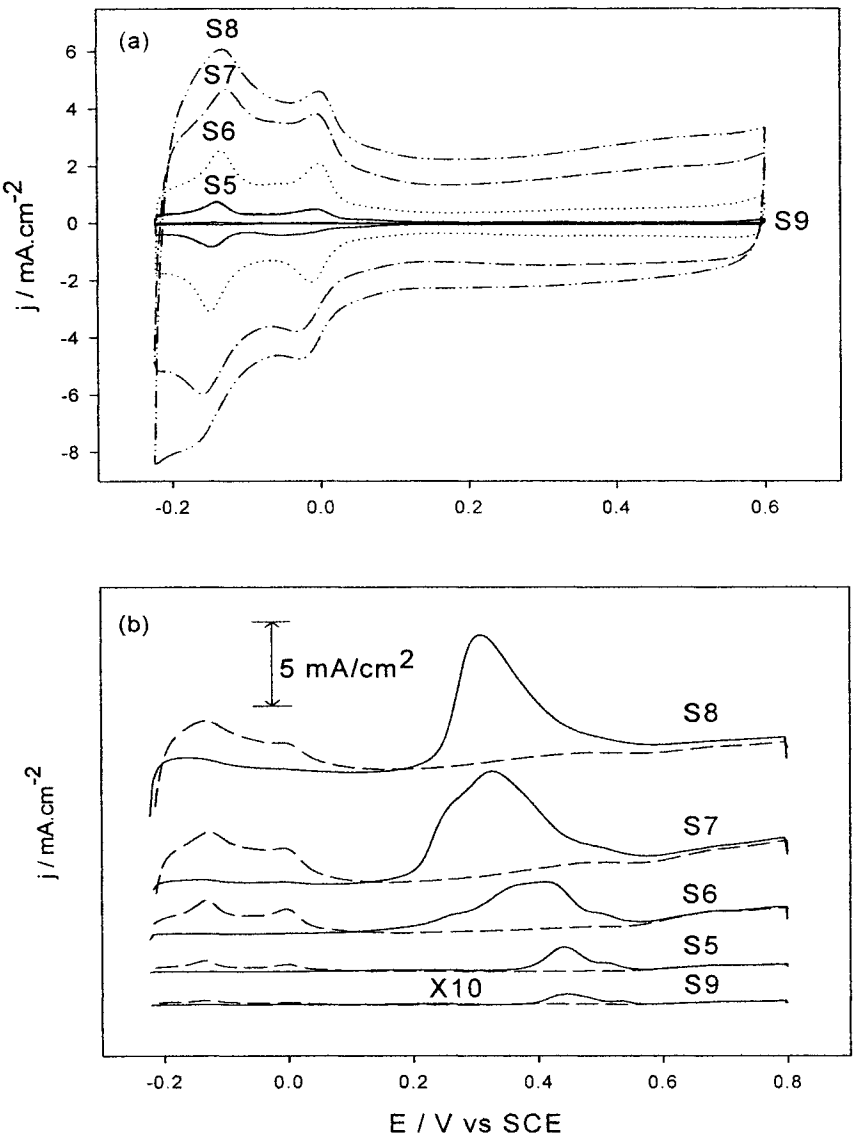

Figure 4.6. (a) Cyclic voltammograms of S5, S6, S7, S8, S9 (Pt Wire); and (b) initial (solid line) and second (dashed line) forward CO oxidation scans. Solution: 0.5 M H_2SO_4; Potential scan rate: 20 mV/s.

A very important factor for the practical use of a DMFC is efficient removal of the CO catalyst poisoning species. Figure 4.6.b shows initial (solid line) and second (dashed line) forward CV scans in 0.5 M H_2SO_4 after purging the solution with CO. All samples show a similar broad peak for the oxidation of CO. The CO oxidation peak is centred around 0.44 V for S9. As the ruthenium concentration increases, the peak is shifted to a lower potential with S8's peak being located at 0.3 V. On the second forward scan, the CO had been completely oxidized and the hydrogen adsorption is no longer suppressed. The charge for the CO oxidation, Q_{CO}, was calculated in a manner similar to that previously mentioned, and once again, the activity of S7 and S8 was well in excess of 100 times that of S9.

4.8 Methanol Oxidation on High Performance PtRu Electrodes

Another important factor involved in DMFCs is the catalyst's activity towards methanol oxidation. Figure 4.7.a shows forward CV curves in a 0.1 M CH_3OH + 0.5 M H_2SO_4 solution at a potential scan rate of 20 mV/s. The onset of methanol oxidation decreases as the ruthenium concentration increases. S7 and S8 showed a very similar active surface as that calculated for the hydrogen adsorption; however, when the ruthenium concentration is past 50% (S8) we observe a decrease in the activity of the sample. This is consistent with previous findings where the maximum activity towards CO oxidation is achieved by a ruthenium concentration of 50% because the number of Pt-Ru neighbours is maximized resulting in more nucleation sites [93]. To study further the activity of the electrodes, chronoamperometry was utilized. Potentials were held at 0.0 V

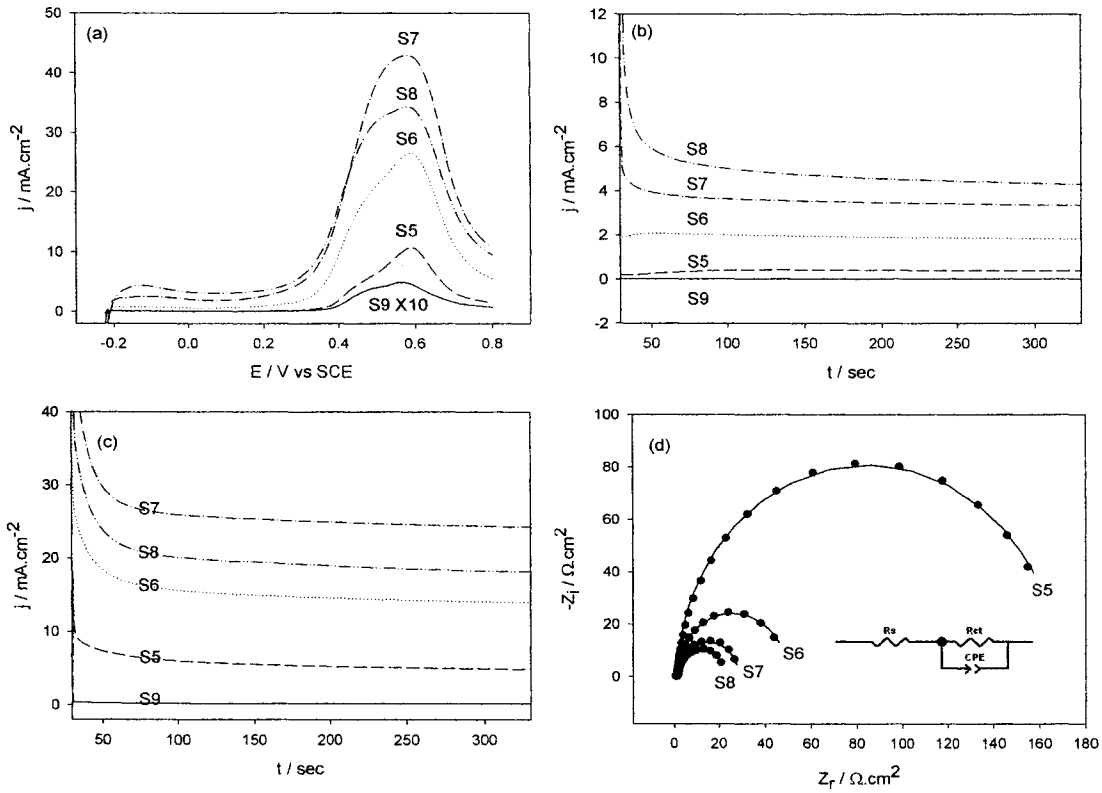

Figure 4.7. (a) Cyclic Voltammograms of S5, S6, S7, S8, S9 in a solution of 0.5 M H_2SO_4 + 0.1 M CH_3OH at a potential scan rate of 20 mV/s, (b) Chronoamperometry at a potential of 300 mV, (c) Chronoamperometry at a potential of 600 mV; and (d) Electrochemical impedance spectra (EIS) at a potential of 300 mV with the equivalent circuit model shown as an inset.

for 30 seconds, and then stepped up to 300 mV and 600 mV respectively (Figure 4.7.b, Figure 4.7.c). Steady-state currents for methanol electrooxidation were achieved after 300 seconds. At a potential of 300 mV, the steady-state currents for S5-S9 are 0.40 $mA.cm^{-2}$, 1.85 $mA.cm^{-2}$, 3.37 $mA.cm^{-2}$, 4.36 $mA.cm^{-2}$ and 0.0143 $mA.cm^{-2}$. Samples S1-S4 all exhibit much higher activities than S5, especially S7 and S8 whose steady state currents are over 200 times that of S9. When a potential of 600 mV, Figure 4.6.c, was used, similar results were achieved with all samples showing superior activity versus polycrystalline Pt. S3 had the highest steady state current at just under 25 $mA.cm^{-2}$. These results are consistent with those shown in Figure 4.7.a. Charge transfer resistance and capacitance measurements were done by way of electrochemical impedance spectroscopy. Figure 4.7.d illustrates four Nyquist plots at a potential of 300 mV in a solution of 0.1 M CH_3OH + 0.5 M H_2SO_4, with the equivalent circuit used for fitting shown as an inset. The real and imaginary components of the impedance are represented by Z_r and Z_i and the shift in frequency is from 40 kHz to 40 mHz. A decrease in size can be easily observed going from sample S5 to S8. The impedance curve representing polycrystalline Pt (S5) and a complete description of the equivalence circuit have been previously reported [40]. Briefly, R_s represents the uncompensated solution resistance, R_{ct} represents the charge transfer resistance and CPE, defined as CPE_T and CPE_P, represents the constant phase element, which takes into account methanol adsorption and oxidation. Samples S5 to S8 all showed a CPE_T value of approximately 0.95 which indicates the CPE_T values are close to the double layer capacitance C_{dl}. The charge transfer resistance for the smallest impedance curve, S8, is 21.92 $\Omega.cm^2$ which is over 325 times smaller than that of polycrystalline Pt (7178 $\Omega.cm^2$). These results show that

the addition of ruthenium to platinum to make 3D nanoporous PtRu alloy network electrodes vastly increases the activity compared to polycrystalline Pt.

4.9 Evaluation of High Performance PtRu Nanomaterials as Glucose Sensors

Nanomaterials with high surface areas have received significant interest due to their unique properties and impressive activities in electrocatalysis. Currently there is a huge interest in developing precise and quick methods to monitor blood sugar levels for the purpose of controlling and treating diabetes. Electrochemical biosensors in particular have received much attention recently for glucose detection due to their quick, concise readings using a disposable tip, which eliminates the possibility of instrument contamination. Nanostructrued Pt-based materials are very attractive due to their excellent electrocatalytical properties.

Electrochemical biosensors for glucose, quite commonly glucose oxidase (GOx), are usually immobilized onto electrodes by covalent attachment, entrapment within a film or by passive adsorption. There have been numerous studies conducted to counter the drawbacks of enzymatic glucose sensing. Disadvantages which exist are enzyme bound electrodes are susceptible to denaturing, poor sensitivity and poor stability. Although the oxidase enzyme is inexpensive, the cosubstrate, oxygen, gets depleted as the sample gets used, resulting in decreased performance. Temperature, chemical and thermal instability, pH and humidity (while in storage or in use) have been shown to be potentially very damaging to enzymatic sensors. The poisoning of the electrode surface by the chloride ion, which is present in physiological conditions (0.1 M), remains a problem for glucose biosensors [5,6,38,39]. An electrode which is capable of sustaining sensitivity and

stability under physiological glucose levels (3-8mM) and in the presence of interfering agents such as L-ascorbic acid is highly desirable.

4.10 Characterization of PtRu Electrodes for Glucose Sensing

Scanning electron microscopy was used to characterize the surface morphologies of 3D nanoporous PtRu alloy network electrodes after hydrothermal treatment. Figure 4.8.a-b show SEM images illustrating excellent coverage of the substrate for samples of NP Pt (S5) and NP Pt/Ru-38% (S7) respectively. The increase in diameter of the porous networks can be readily observed when ruthenium is present along with the platinum, with a range in size from 10's to 100's of nanometers. Further analysis of the sample was done by energy dispersive X-ray spectrometry and X-ray diffraction. Asterisks in Figure 4.8.c-d denote the presence of titanium. The EDS spectrum shown in Figure 4.8.c indicates the presence of ruthenium in S7. XRD patterns in Figure 4.8.d indicate peaks consistent with the face-center-cubic (fcc) pattern anticipated for platinum rich PtRu alloys. A decrease in platinum concentration is observed with the introduction of ruthenium to the sample; however, no diffraction peak for ruthenium is observed which would suggest that a PtRu alloy has been formed on the surface of the sample.

Based on the SEM analysis, we propose a growth method, similar to the seed process previously discussed. At appropriate temperature and pressure, formaldehyde reduces the platinum from Pt^{4+} to Pt^{0} and ruthenium from Ru^{3+} to Ru^{0} resulting in deposition on the titanium substrate surface. As reduction continues, the surface of the substrate gets covered until the nanoparticles start forming on top of one another culminating in the formation of the nanoporous PtRu nanomaterial electrodes.

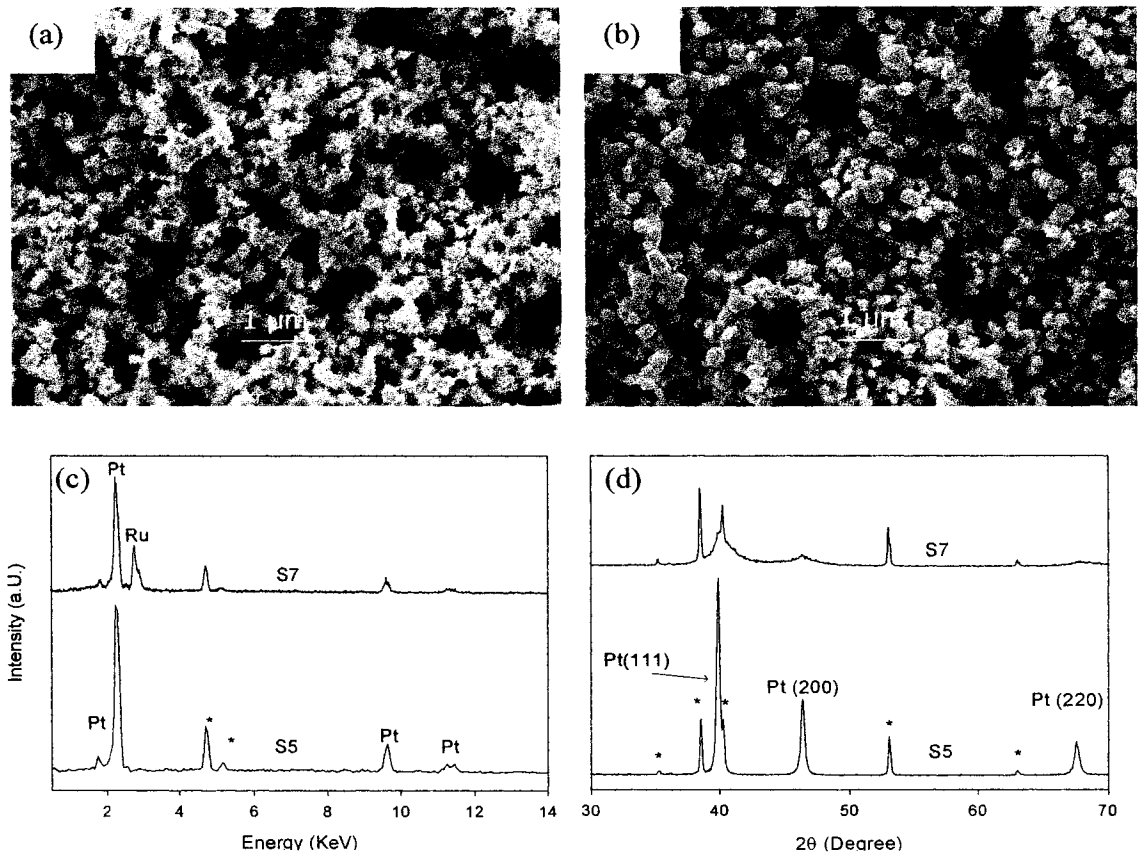

Figure 4.8. SEM Images: (a) Nanoporous Pt (S5); (b) Nanoporous Pt/Ru-38% (S7). The corresponding EDS spectra (c) and XRD patterns (d) of the samples shown in (a) and (b).

4.11 Glucose Oxidation With and Without the Presence of the Chloride Ion

Electrochemical properties of the electrodes were determined by methods including cyclic voltammometry and chronoamperometry. The adsorption and desorption of hydrogen is a very useful method in determining the active surface area of the platinum electrode. In the presence of ruthenium, the double layer capacitance increased while the structure of the hydrogen region became less defined. These observations are consistent with those of Wieckowski's group [90]. Figure 4.9.a shows short range CV scans for polycrystalline Pt, S5 and S7 in a 0.5 M H_2SO_4 solution at a potential scan rate of 20 mV/s. The adsorption/desorption peaks for each sample are consistent with a slight shift from polycrystalline Pt (ca. -0.045 V, -0.185 V) to S7 (ca. -0.077 V, -0.20). The actual surface area of the electrodes is equivalent to the number of Pt sites available for hydrogen adsorption/desorption. We assume the double layer capacitance is constant across the entire potential range when calculating the adsorption charge. The hydrogen adsorption charge (QH) of polycrystalline Pt was calculated at 0.21 mC/cm^2. Samples S5 and S7 produced QH's of 4.85 and 28.48 mC/cm^2. These results show that the active surface area is many times that of polycrystalline Pt, especially with S7 whose actual surface area is well in excess of 100 times greater. Due to the electro-oxidation of glucose on a platinum electrode being kinetically controlled, a Pt or Pt_xM_y electrode with a larger real surface area should have an enhanced glucose oxidation current. Figure 4.9.b shows medium range CV scans for Pt, S5, and S7 in a 5 mM glucose/0.1 M phosphate buffered saline (PBS) solution (pH 7.4, 0.15 M NaCl) at a potential scan rate of 20 mV/s. As seen from Figure 4.8.b, the nanomaterial electrode with the same geometric surface area exhibits vastly superior performance towards glucose oxidation over platinum wire. The

platinum wire shows a small peak for chloride adsorption at a potential of about -0.64 V on the reverse scan and a chloride desorption peak at approximately -0.54 V on the forward scan. In the hydrogen adsorption/desorption region, there is virtually no activity present. There is a small oxidation peak present around 0.55 V which could be attributed to the oxidation of glucose. A small decrease in current observed after the peak may be due to the formation of platinum oxide, which competes with glucose for the adsorption sites on the electrode surface. On the reverse scan the reduction of platinum oxide occurs at approximately 0.18 V, which then frees up sites on the platinum for the adsorption of glucose. When the surface area of the sample is increased, the behavior of the curve is altered. As can be seen in Figure 4.9.b, the nanoporous platinum electrode shows two distinct peaks during the forward scan which are in the negative potential region. These peaks might be the result of the electrosorption of glucose to form an absorbed intermediate releasing one proton per molecule of glucose. The decrease in current after the peaks could be due to the build up of intermediates on the surface of the electrode, which would inhibit further oxidation of glucose. At about 0.3 V there is a peak on the forward scan which could be the result of active sites on the platinum being freed up from the oxidation of glucose derived intermediates by Pt-OH surface species. There is a corresponding reduction peak for Pt-OH on the reverse scan at nearly the same potential. The increase and subsequent decrease in potential following this peak is indicative of glucose being adsorbed causing the current to rise, and intermediates building up causing the current to drop again. A substantial increase in active surface area and capacitance, due to the addition of ruthenium to the sample, culminated in a simpler CV curve which shows 3 current peaks and a larger current range, especially in the positive potential

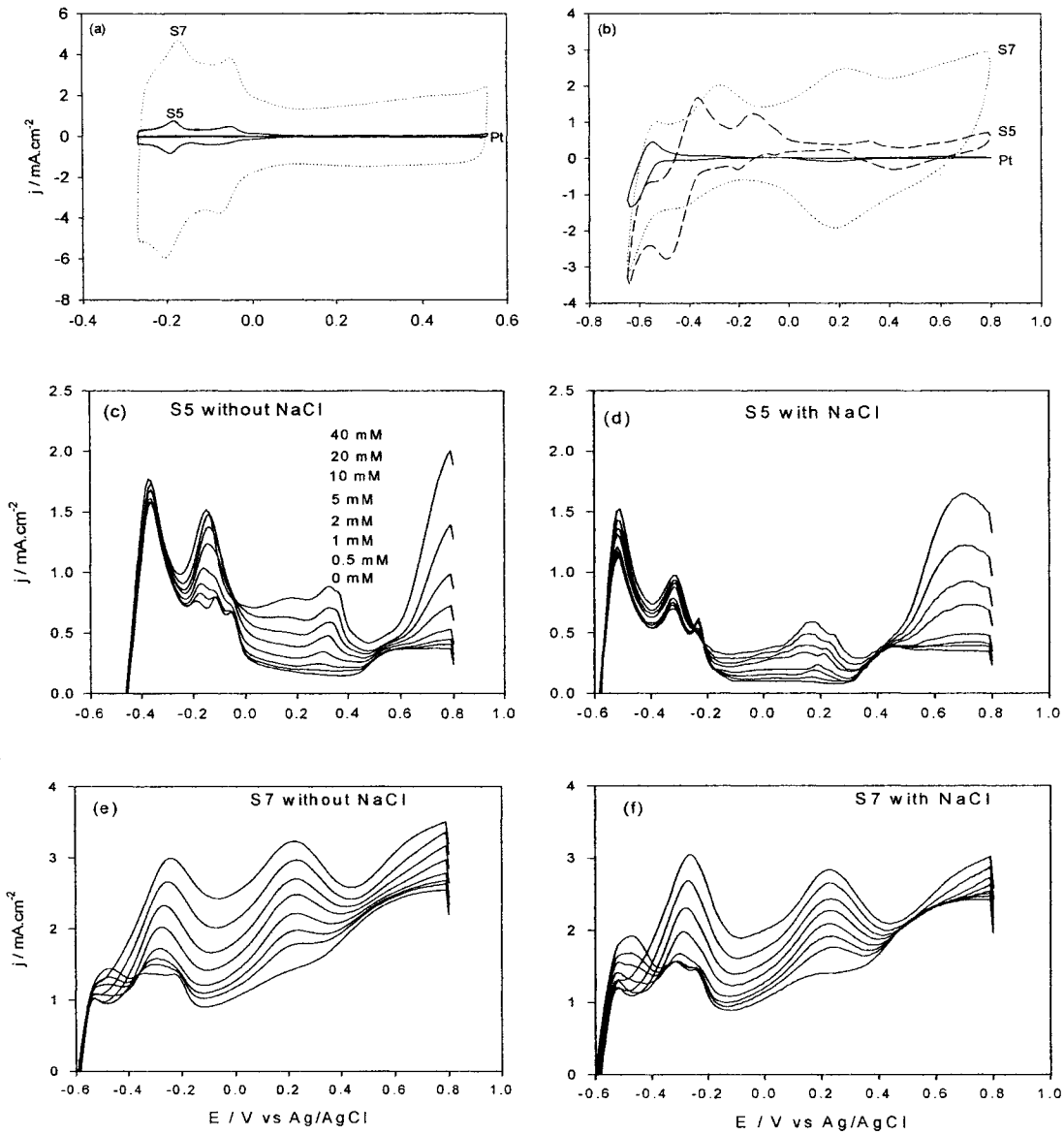

Figure 4.8. (a) Cyclic voltammograms of polycrystalline Pt, S5 and S7 in 0.5 M H_2SO_4 solution; (b) in a 5 mM glucose + 0.15 M NaCl solution; (c) – (f) forward cyclic voltammogram scans of S5 and S7 in a 0.1 M PBS solution (pH 7.4), without/with NaCl at varying concentrations. Potential scan rate: 20 mV/s.

region. The adsorption/desorption peaks, caused in this case by the effect of the Pt-OH and Ru-OH surface species, have shifted to a more negative potential of 0.18 V. Sample S7, containing 38% Ru, exhibits superior performance towards the oxidation of glucose.

A prime poisoning species during glucose sensing, either enzymatic or non-enzymatic in nature, is the presence of the chloride ion. Amperometric signals in the presence of 0.01 M NaCl have been shown to rapidly diminish to near zero levels. Studies have been conducted to counter this by the addition of other metallic species to the platinum electrode [38]. Figure 4.9.c-e shows 4 graphs containing a number of forward CV scans in 0.1 M PBS (pH 7.4) at a potential scan rate of 20 mV/s. A number of concentrations ranging from 0-40 mM glucose with and without NaCl were studied. As seen in Figure 4.9.c-d, sample S5 has a slight reduction of current activity when NaCl is present. The salt also has the effect of shifting the oxidation peaks to more negative potentials. Similar trends are observed for electrode S7 (Figure 4.9.e-f). The nanoporous samples show a small change with/without the presence of the chloride ion, which is an important factor for practical applications as a glucose sensor.

4.12 Glucose Detection Under Physiological Conditions

Chronoamperommetry studies were carried out to determine the potential which would have the best sensitivity towards the detection of glucose. This effect is illustrated in Figure 4.10.a. Potentials ranging from 0.15 V to 0.55 V were tested in a 0.1 M PBS (pH 7.4, 0.15 M NaCl). The potential was held at 0 V for 30 seconds, then stepped up for an additional 150 seconds. A potential of 0.5 V provided the highest steady state current and was therefore chosen for the amperometric studies. The electrocatalytic activity of

the electrodes at a fixed potential and for a time after injections of glucose was studied in order to further evaluate the electrodes sensing ability. Amperometric studies were conducted at 0.5 V in aerated 0.1 M PBS (pH 7.4, 0.15 M NaCl). Stirring was initiated prior to the start of the experiment and remained on throughout. Initially, the potential was held for 1000 seconds and then the first glucose injection was made. The system was then allowed to stabilize for 180 seconds during which time a steady state current was reached. This continued as concentrations of 0, 0.5 and 1-20 mM were studied. Figure 4.10.b shows the amperometric curves for platinum wire and S7. Steady state currents are achieved for both electrodes with the nanoporous $Pt_{62}Ru_{38}$ showing steady state currents at much higher values. In Figure 4.10.c current concentration curves are shown for the three samples tested in this study. The nanomaterial samples show excellent sensitivity towards glucose detection in the physiological range (3 mM – 8 mM). A linear dependence to glucose is observed in the range of 1-17 mM with R values of 0.996 (S5) and 0.999 (S7). Sample S7 shows a sensitivity of 0.022 $mA/cm^2 \cdot mM$ at 6 mM which is over 100 times that of platinum wire at the same concentration. An additional step experiment was performed in the presence of 0.01 mM L-ascorbic acid to evaluate S7's performance with an interfering agent present. Once again the potential was held for 1000 seconds prior to the addition of glucose. This time, though, the interfering agent was injected prior to the glucose injections. Figure 4.10.d shows a current concentration plot with a good linear fit in the 2-8 mM range with an R value of 0.996. Despite the addition of the L-ascorbic acid, the electrode still performed very well in the physiological range.

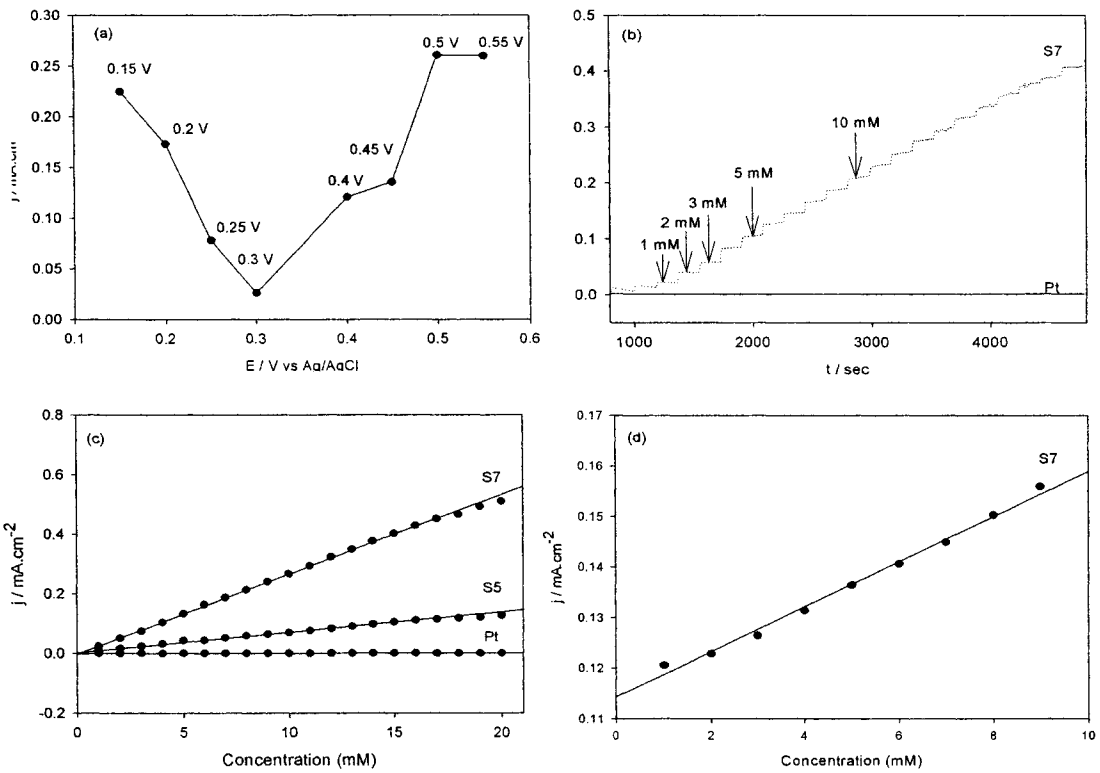

Figure 4.10. (a) Steady-state current responses of S7 in a 0.1 M PBS (pH 7.4, 0.15 M NaCl) solution; (b) Amperometric response of Pt and S7; (c) Calibration curve for amperometric responses of Pt, S5, and S7; and (d) Calibration curve for S7 in the presence of L-ascorbic acid.

4.13 Summary

Nanostructured materials research has garnered a lot of attention due to their unique properties and impressive list of potential applications. Platinum based nanomaterials have shown excellent catalytic activity towards key aspects of the DMFC including hydrogen adsorption/desorption, CO tolerance and methanol oxidation. With their high surface areas, nanoporous Pt materials have shown much improved activity over polycrystalline Pt with activities being as much as 25 times higher. Further enhancement of these electrodes was accomplished by using hydrothermal treatment to disperse a Ru colloid solution into the 3D structure of the Pt electrodes. The result was the formation of 3D NP PtRu electrodes with improved electrocatalytic activity over NP Pt with respect to CO and methanol oxidation. A decrease in the onset potential for CO oxidation and an increase in the peak current density of methanol oxidation (approximately 2 times) was observed with the presence of Ru. In an effort to improve the efficiency of the fabrication process, a simple, one step procedure was developed culminating in the formation of high performance PtRu electrodes. Electrocatalytic performance of these electrodes was vastly superior to the previous samples, especially polycrystalline Pt. As the ruthenium concentration increased, the activity of the electrodes towards hydrogen adsorption/desorption also increased, but the hydrogen region became less structured an increase in capacitance was observed. CO oxidation onset potentials were lowered and the CO was completely oxidized by the second potential sweep cycle. Methanol oxidation currents were significantly improved over the previous method of making NP PtRu electrodes. Activity increased with ruthenium until a concentration of Ru greater then 50% was achieved. The best performing sample had a

Ru concentration of 38% and electrocatalytic activity well in excess of 100 times greater then platinum wire. Further testing of these high performance electrodes was done in a phosphate buffer solution to evaluate their potential as non-enzymatic glucose sensors. Enzymatic glucose sensors are susceptible to a number of negative effects, one of the most prevalent being poisoning of the electrode surface by the chloride ion, as well as interfering agents. Despite the presence of the chloride ion, the PtRu nanomaterial electrodes still showed very good activity towards glucose oxidation. Amperometric studies illustrated that a linear relation could be obtained, especially in the physiological range of 3-8 mM glucose without and with an interfering agent present. These electrodes have shown excellent potential for possible application as glucose sensors.

Chapter 5

Potential Oscillations During the Electrochemical Treatment of White Liquor

5.1 Introduction

White liquor is composed mainly of sodium sulfide, sodium hydroxide and sodium carbonate. The presence of polysulfide in white liquor is known to increase the pulp yield and improve the paper quality in the Kraft process. Electrochemical oxidation of white liquor can generate highly concentrated polysulfide liquor, showing great potential for application in the pulp and paper industry. Sulfide in white liquor is easily oxidized to form polysulfides in the anode compartment at low electrode potential and pure hydrogen is produced as a by-product on the cathode. Pure sodium hydroxide is also recovered in the cathode compartment when a membrane is used to separate the anode and the cathode. Therefore, polysulfide and caustic soda, two very useful chemicals, are produced simultaneously during the electrochemical treatment of white liquor. A dimensionally stable anode (DSA), also referred to as a mixed metal oxide electrode, was used as this type of electrode has yielded good results during the electrochemical treatment of sulfide. The mechanism; however, of sulfide oxidation and soluble polysulfide ions formation, and the nature of the deposited sulfur still need to be clarified.

5.2 Analysis of White Liquor and Characterization of a Ta_2O_5-IrO_2 Electrode

The composition of the white liquor was analyzed using a Varian Vista Pro inductively coupled argon plasma spectrometer (ICAP/ICP). Twenty-six elements (Ag, Al, As, B, Ba, Be, Ca, Cd, Co, Cr, Cu, Fe, K, Mg, Mn, Mo, Na, Ni, P, Pb, Se, Si, Sr, Ti,

V and Zn) were analyzed, but only the elements with a concentration above 5 ppm are shown in Table 5.1. The element with the highest concentration in the white liquor is Na (4.28 M), followed by K and Si. The concentration of hydroxide, sulfide and carbonate was determined using a standard titration analysis of black and white liquors recommended by the Physical and Chemical Standards Committee, Technical Section, Canadian Pulp & Paper Association. The concentration of hydroxide is 2.70 M, the concentration of sulfide is 0.57 M, and the concentration of carbonate is 0.091 M. These results indicate that white liquor possesses very high conductivity and provides an excellent environment for the electrocatalytic production of polysulfide. The surface morphology of the fabricated IrO_2-Ta_2O_5 oxide coating was examined using SEM. Figure 5.1 shows two SEM images of the oxide coating at a low (x 3,000) and a higher magnification (x10,000). The oxide coatings exhibit a typical porous 'cracked mud' structure; sitting on the 'cracked mud' are some oxide particles. This is consistent with the observation by Comninellis et al [95]. These images show that the IrO_2-Ta_2O_5 oxide electrode prepared in this study has a large surface area, which is desirable for industrial electrochemical processes in order to achieve economical performance.

5.3 Cyclic Voltammetry and Linear Galvanic Voltammetry

Cyclic voltammetry (CV) is used for the general characterization of the electrochemical behavior of white liquor on the Ti\IrO_2-Ta_2O_5 oxide electrode. Figure 5.2.a shows two CV curves recorded in the white liquor (solid line) and in a 2.7 M of NaOH (dashed line) solution at a sweep rate of 20 mV/s. As seen in the CV curve of the sodium hydroxide solution, oxygen evolution occurs at about 0.48 V/SCE and, by further

Table 5.1: Composition of the white liquor analyzed using ICP.

Element	Al	B	Ca	Fe	K	Na	P	Pb	Si	Zn
ppm	140	389	42	10	7,976	98,125	23	14	4,672	6

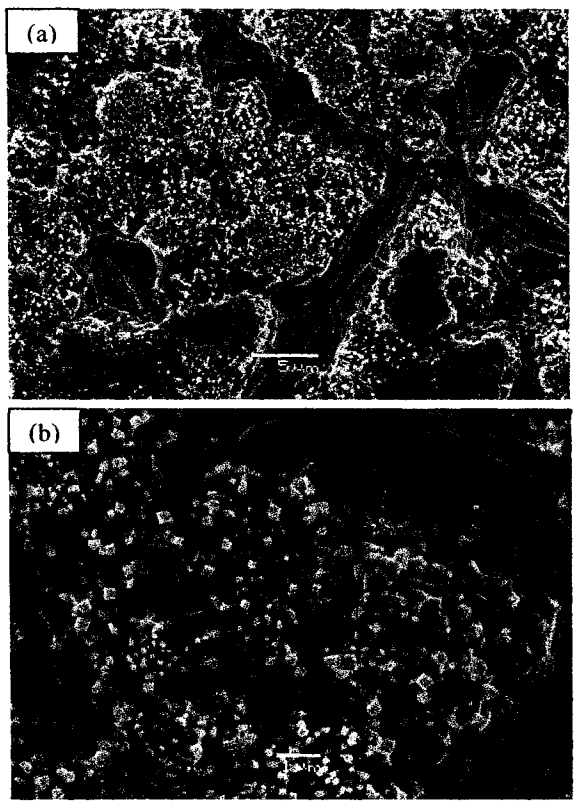

Figure 5.1. SEM images of a Ti/Ta_2O_5-IrO_2 electrode at (a) low magnification, 3 000 X and (b) high magnification, 10 000 X.

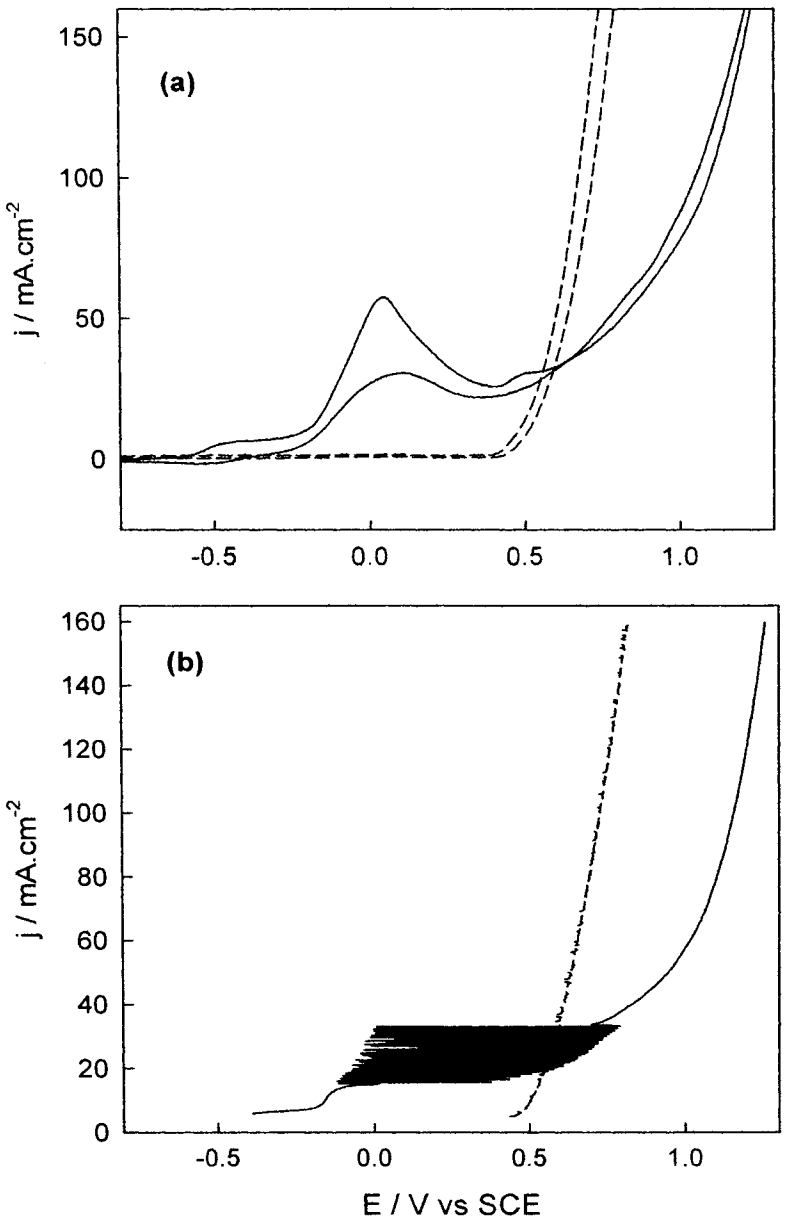

Figure 5.2. (a) Cyclic voltammograms of white liquor (solid line) and 2.7 M NaOH (dashed line) at a potential scan rate of 20 mV/s and (b) Linear galvanic voltammograms of white liquor (solid line) and 2.7 M NaOH (dashed line) with a galvanic scan rate of 20 μA/s.

increasing electrode potential, the current of the oxygen evolution linearly increases. This indicates that the Ti/Ta_2O_5-IrO_2 electrode possesses high electrocatalytic activity for oxygen evolution. In the white liquor (solid line), when sweeping the potential from -1.0 V to 1.5 V/SCE, a broad hump starting at -0.55 V/SCE is observed in the CV, followed by a large and wide peak at around 0.0 V. This may be due to the oxidation of sulfide to polysulfides and sulfur. The broad hump may also be due to sulfide adsorption and/or polysulfide formation [96]. Figure 5.2.b shows two linear galvanic voltammetric (LGV) curves recorded in the white liquor (solid line) and 2.70 M NaOH (dashed line) solutions sweeping from 5 mA to 160 mA at a current scan rate of 20 μA/s. Potential oscillations are observed when the white liquor is used as the electrolyte. The oscillation starts at around 15 mA/cm^2 and vanishes when the current density reaches 35 mA/cm^2. The amplitude of the oscillation depends on the applied current and is located in the potential range from -0.1 to 0.7 V, where sulfide is oxidized to form polysulfides and sulfur as shown in the CV curve (figure 5.2.a). Comparison of the two LGV curves indicates that oxygen evolution is involved in the top portion of the oscillation. Galvanostatic technique was employed to further investigate the oscillation behavior.

5.4 Galvanostatic Potential Oscillations

Figure 5.3 shows six $E \sim t$ curves under different galvanostatic conditions. In each galvanostatic experiment, the initial current density (j_1) is set at 0.0 mA/cm^2 for one minute. The current is then increased to and held at j_2 for 10 minutes. As shown in Figure 5.3.a, at the lowest current density j_2 = 10 mA/cm^2, the electrode potential is around -175 mV and no oscillation is observed. At j_2 = 15 mA/cm^2, when the potential increases from

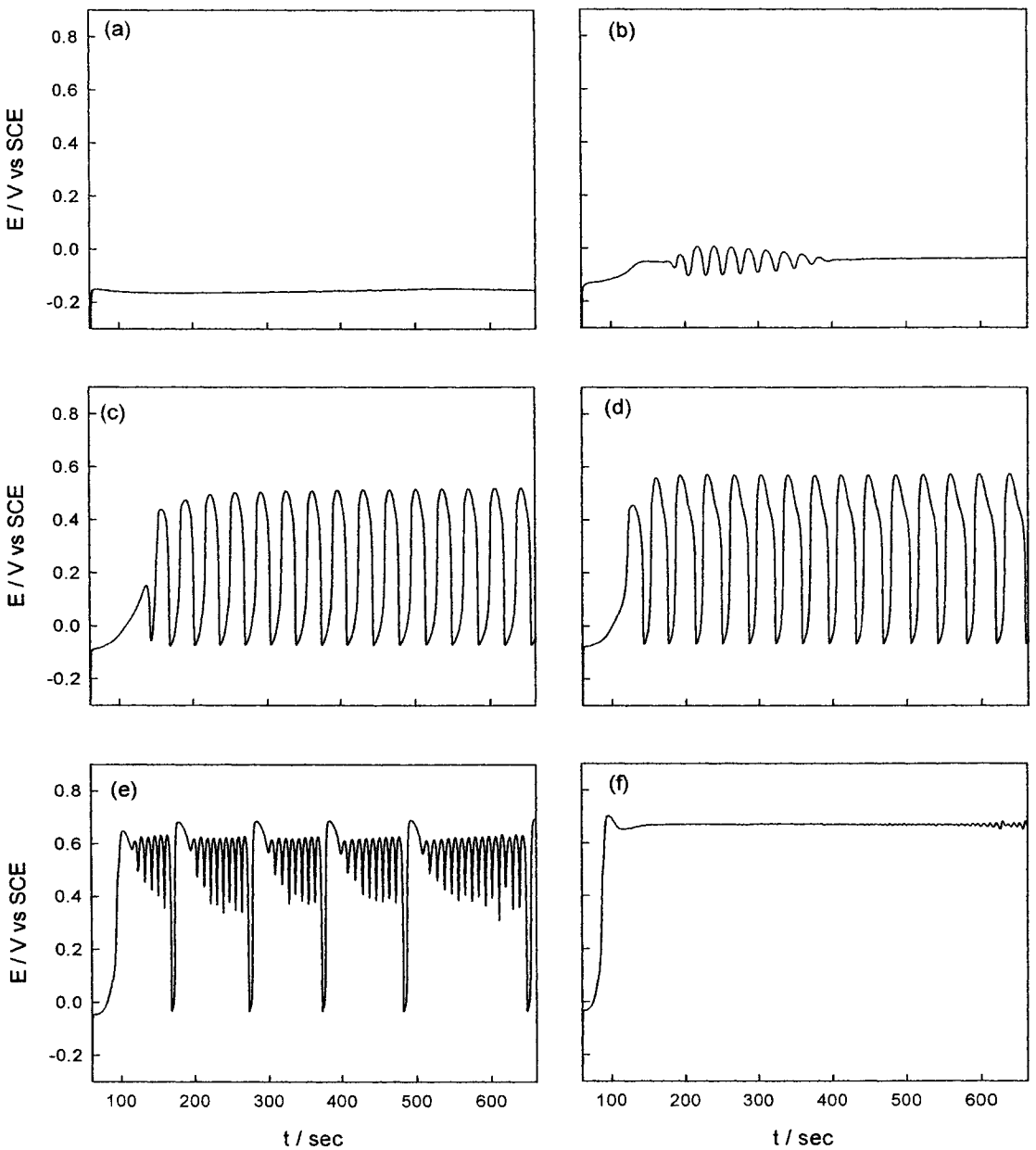

Figure 5.3. Chronopotentiometric curves of white liquor at (a) 10 $mA.cm^{-2}$, (b) 15 $mA.cm^{-2}$, (c) 20 $mA.cm^{-2}$, (d) 22 $mA.cm^{-2}$, (e) 30 $mA.cm^{-2}$, and (f) 35 $mA.cm^{-2}$.

-150 mV to -50 mV, several small oscillations show up; then the oscillation vanishes and the electrode potential stays at around -50 mV. In contrast, harmonic potential oscillations are observed when j_2 is increased to 20 mA/cm^2 (Figure 5.3.c). The amplitude of these oscillations is approximately 600 mV, located between -50 mV and +550 mV. Slightly increasing the current j_2 from 20 to 22 mA/cm^2, relaxation oscillations are observed; there is a shoulder present at around 500 mV when the potential drops from 600 mV to -50 mV. Mixed-mode oscillations with different amplitudes, are observed at 30 mA/cm^2 as shown in Figure 5.3.e. When further increasing the j_2 to 35 mA/cm^2, some very small oscillations are present in the $E \sim t$ curve (Figure 5.3.f). At j_2 = 40 mA/cm^2, potential oscillation disappears, and the electrode potential is around 700 mV. All these results show that the potential oscillations strongly depend on the applied current density. The potential oscillations can be observed when the applied current density is between 15 and 35 mA/cm^2; they disappear when the current is lower than15 mA/cm^2 or higher than 35 mA/cm^2.

5.5. Effect of Stirring/Purging on the Potential Oscillations

Figure 5.4 shows the effect of stirring/purging on the potential oscillations. When the purging/stirring is on or off is marked in each $E - t$ curve. At 20 mA/cm^2, in Figure 5.4.a, purging with ultrapure Ar starts at the bottom of the oscillation; while in Figure 5.4.b,c magnetic stirring is turned on at the top and the bottom part of the oscillation, respectively. All three curves are almost identical, which indicates that the effect of stirring/purging is independent of its start point. With either purging or stirring, the oscillation disappears and the electrode potential stays at around -100 mV. When the

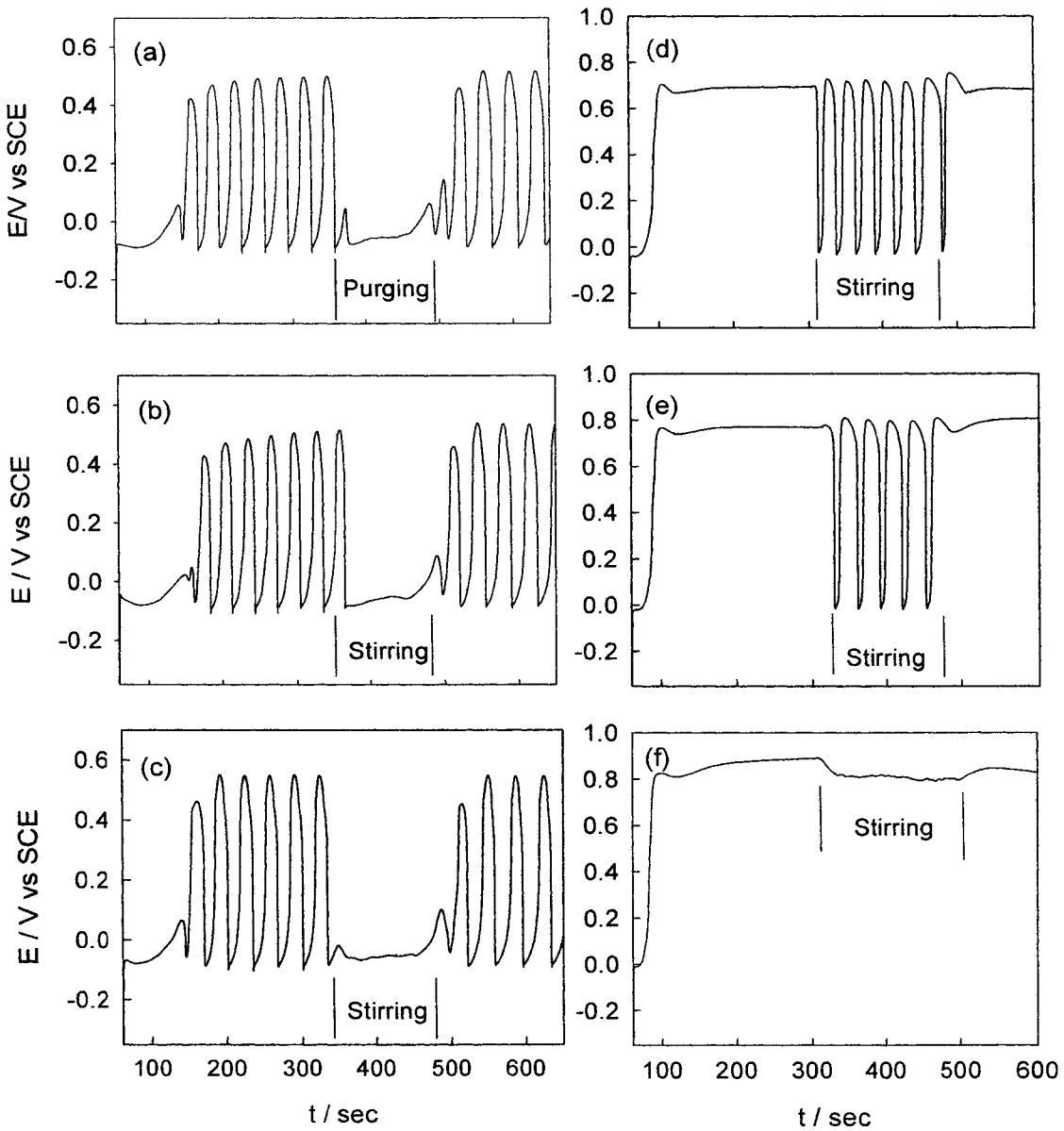

Figure 5.4. Purging/stirring effects on chronopotentiometric curves of white liquor at 22 $mA.cm^{-2}$: (a) purging at top of oscillation, (b) stirring at top of oscillation, (c) stirring at bottom of oscillation, (d) stirring at 35 $mA.cm^{-2}$, (e) stirring at 40 $mA.cm^{-2}$, and (f) stirring at 45 $mA.cm^{-2}$.

purging/stirring is turned off, the potential oscillations recover to their initial behavior. In contrast, it is interesting to notice that harmonic potential oscillations appear when the stirring is turned on at 35 mA/cm^2 (Figure 5.4.d) and 40 mA/cm^2 (Figure 5.4.e). The oscillations vanish when the stirring is turned off. The amplitude of the oscillations at 35 mA/cm^2 shown in Figure 5.4.d is between -20 mV and 700 mV, which is slightly smaller than that shown in Figure 5.4.e at 40 mA/cm^2. The amplitude of the oscillations at 40 mA/cm^2 caused by the stirring is between -20 mV and 780 mV. However, no oscillations are observed at 45 mA/cm^2 (Figure 5.4.f), although the stirring moves the electrode potential from 850 mV down to 800 mV. All the above results show that mass transfer plays an important role in the potential oscillations during the electrooxidation of white liquor.

5.6. Effect of Temperature on the Potential Oscillations

The influence of temperature on the potential oscillation was also investigated in this study. Figure 5.5 presents four LGV curves at different temperatures between 0 and 60°C. The current sweep rate was 20 μA/s. No oscillation is seen at 0°C (Figure 5.5.a). In contrast, potential oscillations are observed at the investigated temperature 20°C, 40°C and 60°C. Increasing temperature increases the onset of current for the potential oscillation. The oscillations start at 15 mA/cm^2 at 20°C, 30 mA/cm^2 at 40°C and 50 mA/cm^2 at 60°C. The inset to Figure 5.5.b shows a portion of the potential oscillations during the period between 300 seconds and 650 seconds at 20 mA/cm^2 and 20°C. The amplitude of the oscillations is 550 mV (between -50 mV and 500 mV) and the frequency is 26 mHz. As shown in the inset to Figure 5.5.c, at 40 mA/cm^2 and 40°C, the amplitude

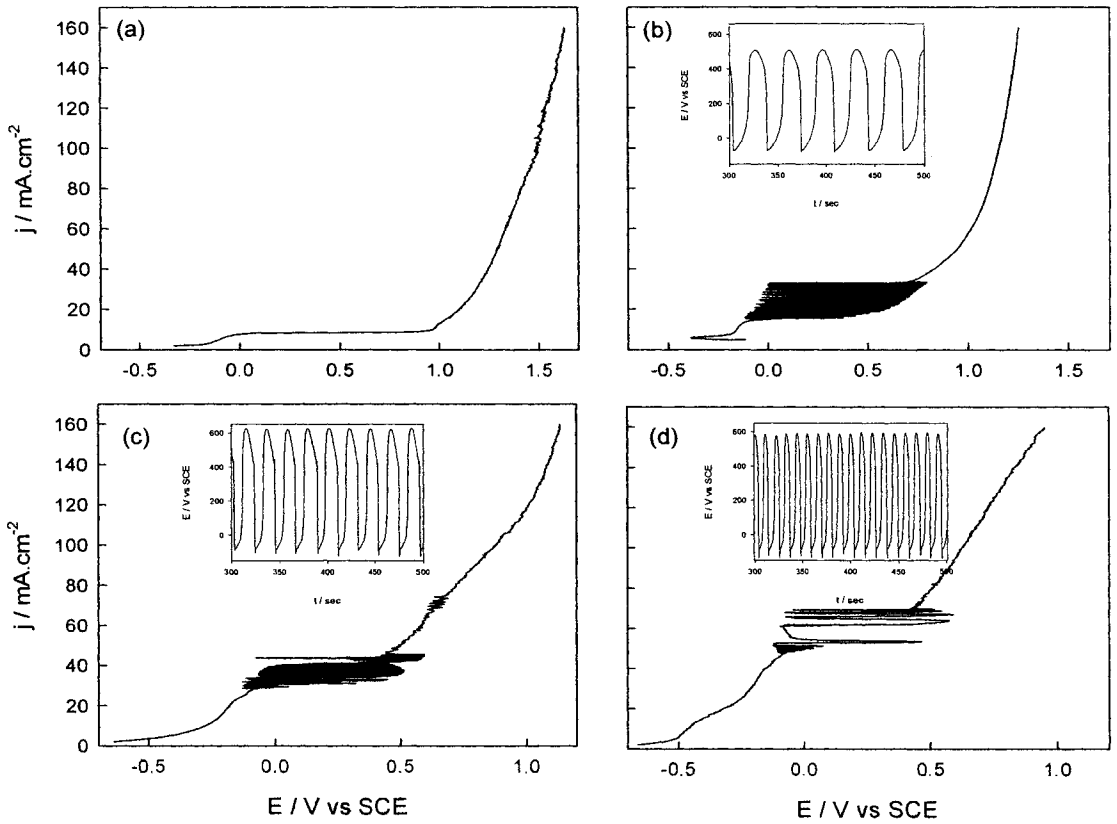

Figure 5.5. Linear galvanic voltammograms of white liquor at (a) 0°C, (b) 20°C, (c) 40°C, and (d) 60°C with a galvanic scan rate of 20 μA/s. The insets to (b), (c), and (d) are chronopotentiometric curves at 20°C and 20 mA/cm^2, 40°C and 40 mA/cm^2, 60°C and 60 mA/cm^2 respectively.

of the oscillations is around 720 mV (between -100 mV and 600 mV), and the frequency of the oscillations is approximately 42 mHz. The inset to Figure 5.5.d presents a portion of the potential oscillations during the period between 300 second and 650 second at 60 mA/cm^2 and 60°C. The amplitude of the oscillations is around 750 mV (between -150 mV and 600 mV) and the frequency is 84 mHz. These results show that the behavior of the potential oscillations strongly depends on the temperature of the white liquor. EIS is a powerful technique in classifying unknown electrochemical oscillators.[62,63] We investigated further using EIS to decipher the nature of the potential oscillations observed in this study.

5.7. Electrochemical Impedance Study and Oscillation Mechanism

Figure 5.6 presents four Nyquist plots recorded in the white liquor at electrode potentials: (a) -150 mV, (b) +200 mV, (c) +550 mV and (d) +800 mV, where Z_r and Z_i are the real and imaginary components of the impedance, respectively. The frequency used in this study was varied from 40 kHz to 40 mHz. The behavior of the impedance plots at +200 mV and +550 mV is dramatically different from the Nyquist plots recorded at −150 mV and +800 mV. Only positive faradic impedance is observed at -150 mV and +800 mV; in contrast, negative real faradic impedance appears at both potentials +200 mV and +550 mV. This is very consistent with the above galvanostatic studies: no potential oscillation is observed at current densities below 15 mA/cm^2 or above 45 mA/cm^2, where the electrode potential is below −150 mV or above 800 mV; in contrast, the amplitude of the observed potential oscillations at room temperature is located between -100 mV and +700 mV. For comparison, we also performed EIS measurements

in 2.7 M NaOH solution, only positive faradic impedance was observed. These results indicate that the negative impedance is caused by sulfur deposits resulted from sulfide oxidation during the electrochemical treatment of the white liquor.

Equivalent electric circuits were used to fit the experimental impedance spectra [97]. The equivalent circuit shown in Figure 5.7.a was used to fit the EIS data presented in Figure 5.6.a and 5.6.d, where only positive faradic impedance was observed; the other equivalent circuit shown in Figure 5.7.b was employed to fit the negative impedance spectra presented in Figure 5.6.b and 5.6.c. All the fitting curves are shown as solid lines together with the experimental data denoted as symbols in Figure 5.6. The excellent fits to the impedance spectra at all four potentials demonstrate the utility of the two equivalent circuits. In both circuits, the R_s represents the uncompensated solution resistance; the parallel combination of the resistance (R_f) and the capacitor (C_f) takes into account the properties of the oxide film [98] and the second parallel combination of RctCPE is associated with the oxidation of sulfide. A CPE is defined by CPE-T and CPE-P. If CPE-P equals 1, then the CPE is identical to a capacitor C. The parallel combination (R_{ct}CPE) leads to a depressed semi-circle in the corresponding Nyquist impedance plot. To account for the negative faradic impedance, another branch consisting of a parallel combination of a capacitor (C1) and a resistor (R1), where R1 is in series with a parallel combination of a resistor (R2) and a capacitor (C2), was included in circuit b. This branch is associated with the formation/removal of sulfur deposits on/from the electrode surface. The values for the parameters determined by the fitting of the experimental EIS data presented in Figure 5.6 using the equivalent electric circuits shown in Figure 5.7 are

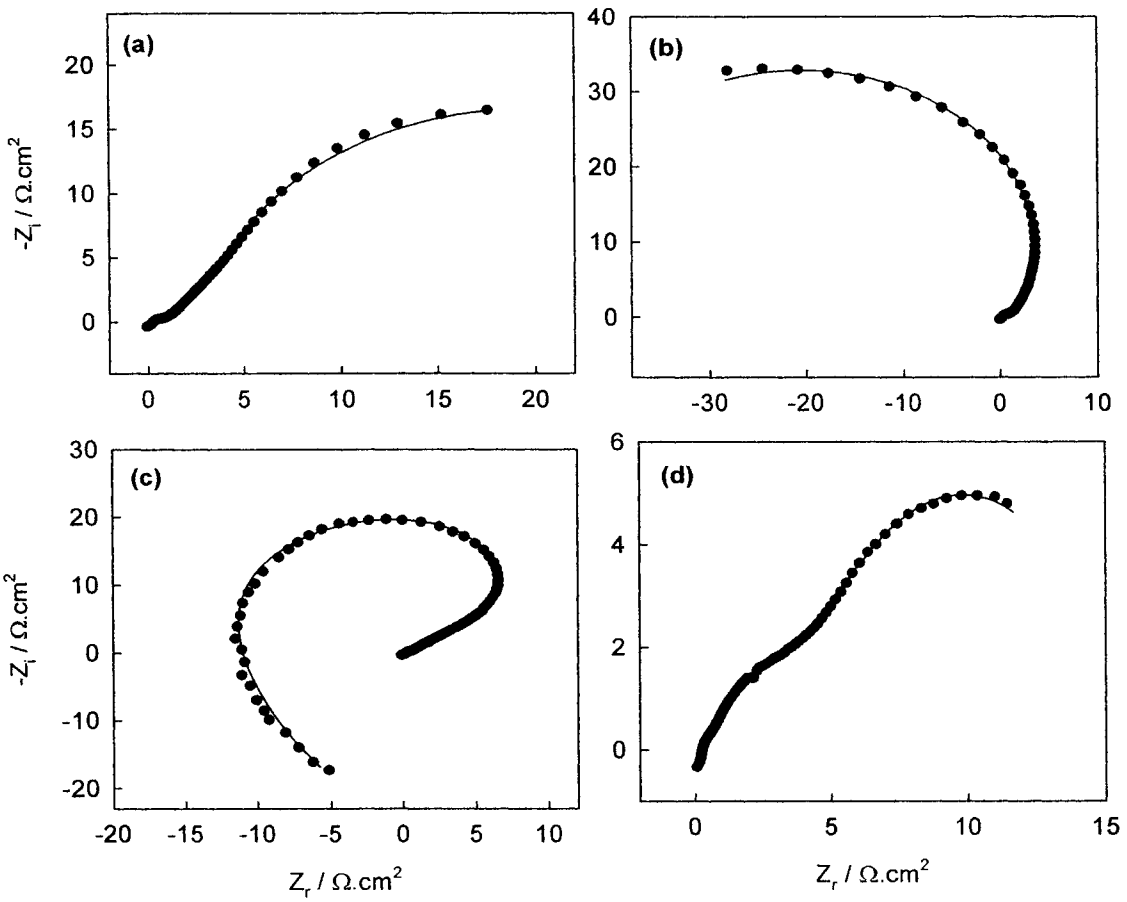

summarized in Table II. R_{ct} is the charge-transfer resistance, and the inverse charge-transfer resistance R_{ct}^{-1} describes how fast the rate of charge transfer changes with a

Figure 5.6. EIS complex plane plots of the Ti/Ta_2O_5-IrO_2 electrode in white liquor at -150 mV, (b) 200 mV, (c) 550 mV and (d) 800 mV.

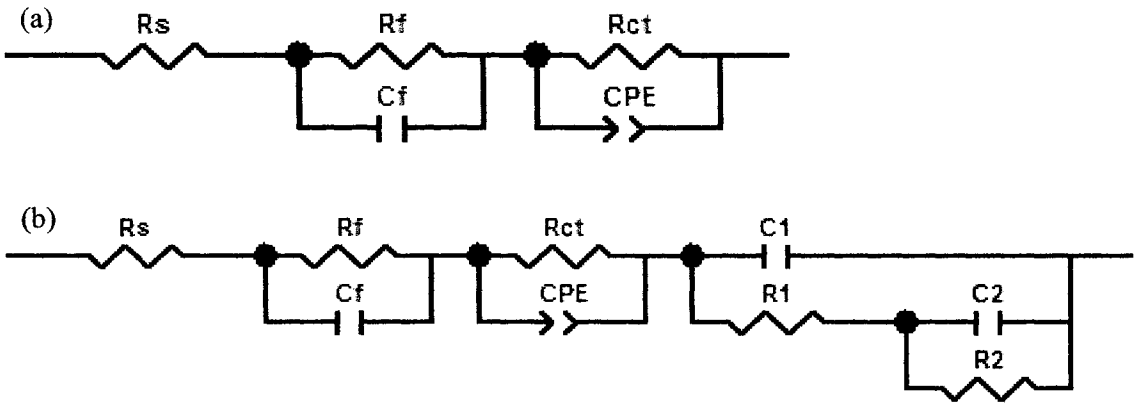

Figure 5.7. Equivalent circuits used to fit experimental data from Figure 4.6 (a) positive impedance (b) negative impedance.

Table 5.2: Impedance components from fitting the experimental EIS data presented in Figure 4.6 using the equivalent electric circuits shown in Figure 5.7.

E	Rf	Cf	Rct	CPE-T	CPE-P	C1	R1	C2	R2
mV	Ω cm^2	mF cm^{-2}	Ω cm^2	mF cm^{-2}		mF cm^{-2}	Ω cm^2	mF cm^{-2}	Ω cm^2
-150	0.4	0.4	20.3	104.4	0.32				
200	0.4	0.2	-25.6	33.4	0.62	2.8	0.4	53.2	-17.9
550	3.7	66.1	-12.6	55.4	0.40	9.0	1.3	-292.2	94.8
800	8.5	19.7	6.5	10.1	0.59				

change in electrode potential, i.e. the potential dependence of the rate constants for charge transfer. As shown in Table 5.2, the R_{ct} at 800 mV is 6.5 Ω cm^2, which is much smaller than the R_{ct} at -150 mV (20.3 Ω cm^2). This is consistent with the observation in the CV studies shown in Figure 5.2.a, where the current density at 800 mV is much higher than that at -150 mV. It is interesting to note that the R_{ct} values at both 200 mV and 550 mV are negative, which indicates that increasing the electrode potential would decrease the current density. This is consistent with the observation of negative faradic impedance at 200 mV and 550 mV.

Anodic oxidation of sulfide can produce elemental sulfur, polysulfides (S_x^{2-}) or sulfur oxyanions depending on the potential, pH and temperature of the electrolyte. Due to the number of different oxidation states associated with sulfur and the complicated composition of white liquor, the mechanistic classification of the electrochemical oxidation of white liquor is quite complex. In what follows, our aim is to explain the occurrence of the oscillation during the electrooxidation of white liquor on the Ti/Ta_2O_5-IrO_2 electrode. Hydrosulfide and sulfide can be oxidized to sulfur and/or polysulfides; sulfide and polysulfides can also be oxidized to form sulfur [70,71]

$HS^- + OH^- \rightarrow S + H_2O + 2\ e^-$ E / V vs SCE -0.478 V (5.1)

$S^{2-} \rightarrow S + 2\ e^-$ E / V vs SCE -0.508 V (5.2)

$2\ S^{2-} \rightarrow S_2^{2-} + 2\ e^-$ E / V vs SCE 0.239 V (5.3)

$S^{2-} + S_2^{2-} \rightarrow S_3^{2-} + 2\ e^-$ E / V vs SCE 0.249 V (5.4)

As shown in Figure 5.3.a, the electrode potential is almost constant, staying at around −180 mV during the 10-minute electrolysis at 10 mA/cm^2. This indicates that there is no sulfur build-up on the electrode surface. As the conductivity of the sulfur layer is very

low, if there were a sulfur layer build-up on the electrode surface, the electrode potential would go up in order to satisfy the applied current. This is also consistent with the fact that only positive impedance is observed at −150 mV (Figure 5.6.a). It has been reported that the sulfur layer can be dissolved by forming polysulfides, i.e.

$$S + HS^- + OH^- \rightarrow S_2^{2-} + H_2O \quad (5.5)$$

$$S + S_2^{2-} \rightarrow S_3^{2-} \quad (5.6)$$

The rate of sulfur dissolution in the presence of HS^- and OH^- ions is expected to be enhanced with increasing pH according to Reaction 5.5. The hydroxide concentration in the white liquor is very high (2.7 M). Thus, although there is sulfur formation even at low electrode potential (Reaction 5.1 and 5.2), one would not see sulfur build-up on the electrode surface if the dissolution of sulfur (Reaction 5.5 and 5.6) is faster than its formation. This is also supported by the results shown in Figure 5.4.a-c: the potential oscillations vanish and the electrode potential stays at around -100 mV when the stirring or the purging is turned on. The stirring/purging increases the mass transfer of HS^-, S^{2-} and OH^- from the bulk electrolyte to the electrode surface, which promotes Reaction 5.5. The production of polysulfide S_2^{2-} in Reaction 5.5 catalyzes Reaction 5.6 to accelerate the dissolution of the sulfur deposits by forming polysulfides. Thus, there is no sulfur build-up on the electrode surface due to the stirring or purging, and the potential oscillations vanish. This indicates that the potential oscillations are associated with the periodic formation/removal of a sulfur layer. No periodic sulfur formation/removal is observed at the low temperature 0°C, which is why we do not see any oscillations in Figure 5.5.a. In addition, at the high current densities 35 and 40 mA/cm^2, the potential stays above 700 mV because of sulfur deposits and no oscillation is observed in Figure 5.3.f; however,

one can see strong potential oscillations in Figure 5.4.d-e with the stirring. The convection induced by the stirring or purging results in the removal of the sulfur deposits from the electrode surface.

As seen in Figure 5.3.c-d, the amplitude of the oscillation is between -50 and 600 mV. Oxygen evolution is present at the upper side of the oscillation, while it stops at the lower potential side based on the experiment results above (Figure 5.2.a-b), i.e., periodic oxygen evolution occurs during the oscillation when the potential is higher than 450 mV. As seen in Figure 5.3.d, harmonic potential oscillations are observed at 22 mA/cm^2. At the bottom part of the oscillations, the predominant reaction is sulfide oxidation to form sulfur. Indeed, we did observe sulfur deposits form on the electrode surface. Because of the sulfur deposited on the electrode surface, electrode potential goes up. As shown in Figure 5.2, oxygen evolution strongly depends on the applied potential. When the electrode potential increases, oxygen evolution significantly increases. Thus, at the top part of the oscillations, oxygen evolution becomes the predominant reaction where we observe gas evolution, i.e. much less sulfur is produced at the top part of the oscillations than that at the bottom of the oscillations as the applied current is constant; therefore, more HS^-/S^{2-} are used for sulfur dissolution (Reaction 5.5 & 5.6) at the top part of the oscillation than at the bottom of the oscillation. Furthermore, the oxygen evolution increases mass transport, thus, more HS^-/S^{2-} are available for sulfur dissolution (Reaction 5.5 & 5.6). Actually, we observed partial removal of sulfur deposits periodically from the electrode surface during the experiments. The potential oscillations are thus caused by the synergic effect of sulfur formation/removal and oxygen evolution in the high potential range.

5.8 Summary

The electro-oxidation of white liquor on the Ti/Ta_2O_5-IrO_2 oxide electrode has been investigated by a number of electrochemical methods such as cyclic voltammetry, differential capacity, galvanostatic measurements and electrochemical impedance spectroscopy. The composition of the white liquor is analyzed using ICP. Sodium is the highest concentration (4.28 M) in the white liquor, followed by K and Si. The concentration of hydroxide is 2.70 M, the concentration of sulfide is 0.57 M, and the concentration of carbonate is around 0.091 M. White liquor provides an ideal environment for electrolytic polysulfide production due to its very high conductivity. The SEM analysis shows that the Ti/Ta_2O_5-IrO_2 electrode prepared in this study has a 'cracked mud' structure with oxide particles sitting on the top. Galvanostatic potential oscillations are observed during the electro-oxidation of the white liquor on the oxide electrode. The potential oscillations strongly depend on the applied current density, temperature and mass transfer. Negative faradic impedance is observed in the potential range of the potential oscillation amplitude. The oscillation is associated with the formation/removal of the sulfur deposits. The potential oscillations are caused by the synergic effect of sulfur formation/removal and oxygen evolution at the high potential range. We are further studying the effect of the potential oscillations on the lifetime of Ti/Ta_2O_5-IrO_2 electrodes during electrochemical treatment of white liquor.

Chapter 6

Summary

Nanostructured materials with high active surface areas possess unique chemical and physical properties which haves made them very attractive towards the development of fuel cells, catalysts and, chemical sensors, and the study of non linear chemical dynamics. In this work, a number of novel Pt-based and IrO_2-based nanomaterials were prepared. All were characterized using a wide range of surface analysis techniques and electrochemical methods. The following summarizes the major results obtained during the course of this work.

6.1 Three-dimensional nanoporous Pt and Pt-based Materials

Three Dimensional (3D) nanoporous Pt and Pt-based materials with high active surface areas were fabricated on Ti substrates using a combination of electrochemical deposition and/or hydrothermal method. SEM analysis showed that 3D nanostrutured networks of Pt had been formed on the surface of the substrate. EDS spectra confirmed that the network material deposited on the surface was Pt. XRD patterns indicated that aside from one PtRu sample (Ru-59%), alloys were formed as there was not visible diffraction peak for Ru present in the spectra. Hydrogen adsorption/desorption is recognized as a powerful method for calculating the active surface area of platinum electrodes [91]. In calculating the hydrogen adsorption charge on electrode surfaces, an assumption is made that the double layer charging is constant over the whole potential range. Figure 6.1.a shows CV curves for polycrystalline Pt, NP Pt made from electrochemical deposition and hydrothermal

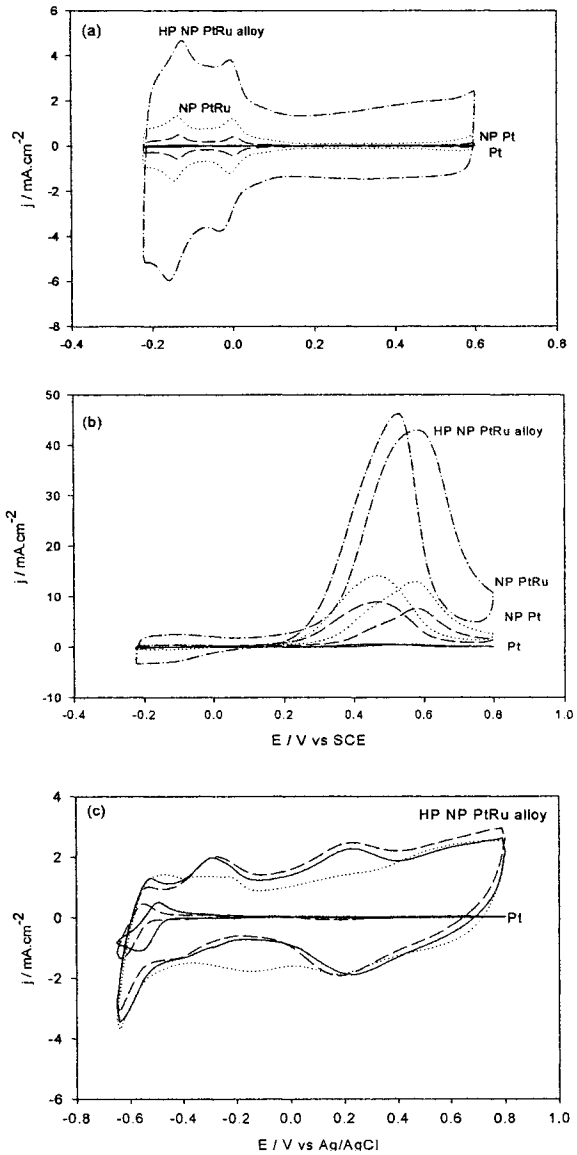

Figure 6.1. (a) Cyclic voltammograms of various Pt-based samples in 0.5 M H_2SO_4 at a potential scan rate of 20 mV/s, (b) cyclic voltammograms of the Pt-based samples in 0.5 M H_2SO_4 + 0.1 M CH_3OH at a potential scan rate of 20 mV/s and (c) cylic voltammograms of polycrystalline Pt and a HP NP PtRu alloy in a 0.1 M PBS buffer solution, dotted lines, 5 mM glucose without 0.15 M NaCl, dashed lines, and 5 mM glucose with 0.15 M NaCl, solid lines.

treatment, NP PtRu made from electrochemical deposition and hydrothermal treatment and a high performance PtRu alloy made from a single hydrothermal treatment. The electrolyte used was 0.5 M H_2SO_4 and the potential scan rate was 20 mV/s. The hydrogen adsorption/desorption charge on the polycrystalline Pt suface shown in Figure 1a is around 0.21 mC/cm^2. In contrast, the nanoporous Pt showed a significant increase in active surface area with a hydrogen desorption charge of 4.13 mC/cm^2. The addition of Ru to the 3D Pt increased the double layer charging and bumped the hydrogen desorption charge to 8.29 mC/cm^2. A high performance PtRu alloy sample (Ru-38%) produced massive increases in capacitance and hydrogen adsorption/desorption. The hydrogen desorption charge calculated for this sample is 28.48 mC/cm^2, which is over 100 times larger than the smooth polycrystalline Pt surface. Their electro-catalytic activity towards methanol oxidation is shown in Figure 6.1.b. The 3D electrodes give a much higher response to methanol oxidation thaen the polycrystalline Pt electrode as well as lower the onset potential. Ruthenium addition, up to 50%, greatly enhances the activity of Pt catalysts by increasing the number of Pt-Ru neighbours resulting in more nucleation sites. The high performance nanoporous PtRu alloy shows a very low onset potential for methanol oxidation, 0.15 V, and a vastly higher current density compared to the rest of the samples. Further testing of the high performace PtRu alloy was conducted for the development of non-enzymatic glucose sensors. Figure 6.1.c shows CV curves for polycrystalline Pt and PtRu-38% in the presence or in the absence of chloride ions. A 0.1 M PBS (pH 7.4, 0.15 M NaCl) solution containing 5 mM of glucose was also tested. Oxidation current for glucose remained quite high, in the mA/cm^2 range. Good sensitivity, especially in

the presence of the chloride ion, is important for glucose sensing as chloride has been shown to poison enzymatic and non-enzymatic sensors, greatly reducing their activity. In contrast, our experimental results have demonstrated that the presence of chloride ions, only slightly decreases the current density of glucose oxidation on the 3D PtRu electrode fabricated in this study.

6.2 Electrochemical Oscillations during the Oxidation of White Liquor

Polysulfide enhanced white liquor has been shown to increase the pulp yield during the kraft pulping process and to improve the quality of the paper produced. White liquor is composed of mainly sodium sulfide, sodium hydroxide and sodium carbonate. During this study, we have also studied electrochemical treatment of white liquor using Ti/Ta_2O_5-IrO_2 electrodes. Figure 6.2.a shows a LGV study in a white liquor sample obtained from a local pulp and paper mill. Linear galvanic voltammetry produced harmonic potential oscillations ranged from -150 mV to +750 mV/SCE. The current range of these oscillations was from 15 mA/cm^2 to 35 mA/cm^2. Further galvanostatic studies of the oscillations indicated that their behavior was strongly dependent on the applied current density, mass transfer and temperature. Electrochemical impedance spectroscopy was employed to study the origin of the oscillations during the electrochemical treatment of the white liquor. The EIS curve in Figure 6.2.b was recorded at a potential of 700 mV/SCE. Negative faradic impedance is observed in the potential range of the potential oscillation amplitudes, and equivalent electric circuits were designed to fit the experimental impedance spectra. This type of oscillator can be classified a Hidden Negative Differential

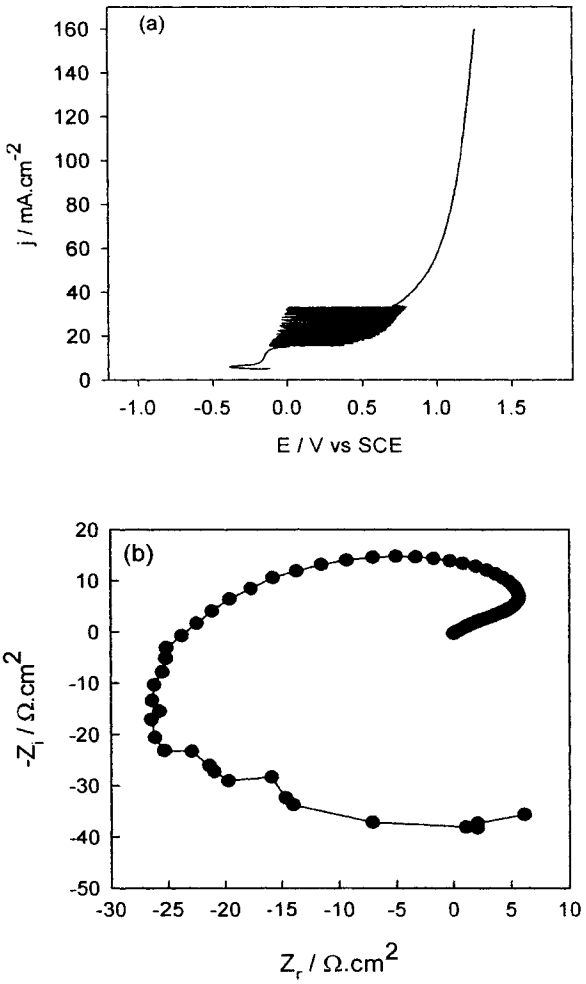

Figure 6.2. (a) Linear galvanic voltammogram of Ta_2O_5-IrO_2 in white liquor at a sweep rate of 20 $\mu A/cm^2$ and (b) EIS spectrum of Ta_2O_5-IrO_2 in white liquor at a potential of 700 mV.

Resistance (HNDR) oscillator with oxygen evolution involved. The potential oscillations are caused by the synergic effect of sulfur formation/removal and oxygen evolution in the high potential range.

In summary, activities towards methanol oxidation and non-enzymatic glucose sensing have been significantly enhanced by the development of novel nanoporous 3D Pt-based materials while polysulfide enriched white liquor was produced with IrO_2 based electrodes and electrochemical treatment.

References:

(1) Lu, Y.; Wang, Q.; Sun, J.; Shen, J. *Langmuir* **2005**, *21*, 5179.

(2) Lu, Q.; Yang, B.; Zhuang, L.; Lu, J. *J. Phys. Chem. B* **2005**, *109*, 1715.

(3) Bock, C.; Paquet, C.; Couillard, M.; Botton, G.A.; MacDougall, B.R. *J. Am. Chem. Soc.* **2004**, *126*, 8028.

(4) Spinacé, E.V.; Neto, A.O.; Linardi, M. *J. Power Sources* **2004**, *129*, 121.

(5) Park, S.; Chung, T.D.; Kim, H.E. *Anal. Chem.* **2003**, *75*, 3046.

(6) Yuan, J.; Wang, K.; Xia, X. *Adv. Func. Mater.* **2005**, *15*, 803.

(7) Arnold, M.A.; Small, G.W. *Anal. Chem.* **2005**, *77*, 5429.

(8) Lee, J.; Park, S-M. *Analytica Chimica Acta*, **2005**, *545*, 27.

(9) Hrapovic, S., Luong, J.H.T. *Anal. Chem.* **2003**, *75*, 3308.

(10) Barone, P.W.; Parker, R.S.; Strano, M.S. *Anal. Chem.* **2005**, *77*, 7556.

(11) Hudson, J.L.; Tsotsis, T.T. *Chem. Eng. Sci.* **1994**, *49*, 1493.

(12) Lamy, C.; Léger, J-M. *Interfacial Electrochemistry* Wieckowski, A. (Ed.) Dekker, M. New York, **1999**, *48*, 885.

(13) Wagner, N.; Schulze, M. *Electrochimica Acta* **2003**, *48*, 3899.

(14) Yu, E.H.; Scott, K.; Reeve, R.W. *J. Electroanal. Chem.* **2003**, *547*, 17.

(15) Lizcano-Valbuena, W.H.; Paganin, V.A.; Gonzalez, E.R. *Electrochimica Acta* **2002**, *47*, 3715.

(16) Gottesfield, S.; Zawodzinski, T.A. *Advances in Electrochemical Science and Engineering* Alkire, R.C.; Gerischer, H.; Kolb, D.M.; Tobias, C.W. (EDs.) Wiley-VCH, New York, **1997**, *5*, 195.

(17) Jambunathan, K.; Jayaraman, S.; Hillier, A.C. *Langmuir* **2004**, *20*, 1856.

(18) Ramya, K.; Dhathathreyan, K.S. *J. Electroanal. Chem.* **2003**, *542*, 109.

(19) Hoster, H.; Iwasita, T.; Baumgartner, H.; Vielstich, W. *Phys. Chem. Chem. Phys.* **2001**, *3*, 337.

(20) Hamnett, A. *Interfacial Electrochemistry* Wieckowski, A. (Ed.) Dekker, M. New York, **1999**, *47*, 843.

(21) Jiang, J.; Kucernak, A. *Chem. Mater.* **2004**, *16*, 1362.

(22) Yang, B.; Lu, Q.; Wang, Y.; Zhuang, L.; Lu, J.; Liu, P. *Chem. Mater.* **2003**, *15*, 3552.

(23) Coutanceau, C.; Rakotondrainibé, A.F.; Lima, A.; Garnier, E.; Pronier, S.; Léger, J-M.; Lamy, C. *J. Appl. Electrochem.* **2004**, *34*, 61.

(24) Sirk, A.H.C.; Hill, J.M.; Kung, S.K.Y.; Birss, V.I. *J. Phys. Chem. B.* **2004**, *108*, 689.

(25) Frelink, T.; Visscher, W.; Van Veen, J.A.R. *Langmuir* **1996**, *12*, 3702.

(26) Liu, Z.; Lee, J. Y.; Chen, W.; Han, M.; Gan, L. M. *Langmuir.* **2004**, *20*, 181.

(27) Denis, M.; Gouérec, P.; Guay, D.; Dodelet, J.; Lalande, G.; Schulz, R. *J. Appl. Electrochem.* **2000**, *30*, 1243.

(28) Iwasita, T.; Hoster, H.; John-Anacker, A.; Lin, W.; Vielstich, W. *Langmuir*, **2000**, *16*, 522.

(29) Rice, C.; Tong, Y.; Oldfield, E.; Wieckowski, A.; Hahn, F.; Gloaguen, F.; Léger, J.; Lamy, C. *J. Phys. Chem. B.* **2000**, *104*, 5803.

(30) Liu, Z.L.; Lin, X.Y.; Lee, J.Y.; Su, X.D.; Gan, L.M. *J. Mater. Chem.* **2003**, *13*, 3049.

(31) Hogarth, M.P.; Ralph, T.R. *Platinum Metals Rev.* **2002**, *46*, 146.

(32) Nashner, M.S.; Frenkel, A.I.; Somerville, D.; Hills, C.W.; Shapley, J.R.; Nuzzo, R.G. *J. Am. Chem. Soc.* **1998**, *120*, 8093.

(33) Hills, C.W.; Nashner, M.S.; Frenkel, A.I.; Nuzzo, R.G. *Langmuir* **1999**, *15*, 690.

(34) Sun, Y.; Buck, H.; Mallouk, T.E. *Anal. Chem.* **2001**, *73*, 1599-1604.

(35) Newman, J.D.; Turner, A.P.F. *Biosensors and Bioelectronics* **2005**, *20*, 2435.

(36) Canadian Diabetes Association

(37) Medical Dictionary

(38) Park, S.; Boo, H.; Chung, T.D. *Analytica Chimica Acta* **2006**, *556*, 46-57.

(39) Boo, H.; Park, S.; Ku, B.; Kim, Y.; Park, J.H.; Kim, H.C.; Chung, T.D. *J. Am. Chem. Soc.* **2004**, *126*, 4524-4525.

(40) Chen, A.; La Russa, D.J.; Miller, B. *Langmuir* **2004**, *20*, 9695.

(41) Song, Y-Y.; Zhang, D.; Xia, X-H. *Chem. Eur. J.* **2005**, *11*, 2177-2182.

(42) Vassilyev, Y.B.; Khazova, O.A.; Nikolaeva, N.N. *J. Electroanal. Chem.* **1985**, *196*, 105.

(43) Wittstock, G.; Strübing, A.; Szargan, R.; Werner, G. *J. Electroanal. Chem.* **1998**, *444*, 61.

(44) Zhang, X.; Chan, K-Y.; You, J-K.; Lin, Z-G.; Tseung, A.C.C. *J. Electroanal. Chem.* **1997**, *430*, 147.

(45) Hedges, E.S.; Meyers, J.E. *The Problem of Physico-chemical Periodicity* Arnol, London, **1926**.

(46) Wojtowicz, J.; Marincic, N.; Conway, B.E. *J. Chem. Phys.* **1968**, *48*, 4333.

(47) Schell, M.; Albahadily, F.N.; Safar, J.; Xu, Y. *J. Phys. Chem.* **1989**, *93*, 4806.

(63) Koper, M.T.M. *J. Electroanal. Chem.* **1996**, *409*, 175.

(64) Koper, M.T.M. *Electrochimica Acta* **1992**, *37*, 1771.

(65) Dorris, G.M. *Pulp & Paper Canada* **1994**, *95*, 394.

(66) Kleppe, P.J.; Minja, R.J.A.

(67) Behm, M.; Simonsson, D. *J. App. Electrochem.* **1997**, *27*, 507.

(68) Behm, M.; Simonsson, D. *J. App. Electrochem.* **1999**, *29*, 521.

(69) Watanabe, K.; Shimizu, M.; Nanri, Y.; Andoh, T.; Shimohira, T. *Tappi*, **2001**, *84*, 48.

(70) Latimer, W.M. *The Oxidation States of the Elements and Their Potentials in Aqueous Solutions* 2nd Ed., Prentice Hall, Inc., Englewood Cliffs, N.J. **1952**.

(71) Szynkarczuk, J.; Komorowski, P.G.; Donni, J.C. *Electrochimica Acta* **1994**, *40*, 487.

(72) Ateya, B.G.; Al-Kharafi, F.M. *Electrochem. Commum.* **2002**, *4*, 231.

(73) Szynkarczuk, J.; Komorowski, P.G.; Donini, J.C. *Electrochim. Acta* **1994**, *39*, 2285.

(74) Helms, H.; Schlomer, E.; Jansen, W. *Monatsh. Chem.* **1998**, *129*, 617.

(75) Buckley, A.N.; Hamilton, I.C. *J. Electroanal. Chem.* **1987**, *216*, 213.

(76) Chen, A.; Miller, B. *J. Phys. Chem. B.* **2004**, *108*, 2245.

(77) Miller, B.; Chen, A. *Electrochimica Acta* **2005**, *50*, 2203.

(78) Berlouis, L.E.A.; Elfick, P.V.E.; Tarry, H. *J. Chem. Soc. Faraday Trans.* **1997**, *93*, 2291.

(79) Chen, A.; Shi, Z.; Bizzotto, D.; Lipkowski, J.; Bilger, C. *J. Electroanal. Chem.* **1999**, *467*, 342.

(48) Schmidt, T.J.; Grgur, B.N.; Markovic, N.M.; Jr. Ross, P.N. *J. Electroanal. Chem.* **2001**, *500*, 36.

(49) Strasser, P.; Eiswirth, M.; Ertl, G. *J. Chem. Phys.* **1997**, *107*, 991.

(50) Lee, J.; Christoph, J.; Strasser, P.; Eiswirth, M.; Ertl, G. *Phys. Chem. Chem. Phys.* **2003**, *5*, 935.

(51) Krausa, M.; Vielstich, W. *J. Electroanal. Chem.* **1995**, *399*, 7.

(52) Wolf, W.; Lübke, M.; Koper, M.T.M.; Krischer, K.; Eiswirth, M.; Ertl, G. *J. Electroanal. Chem.* **1995**, *399*, 185.

(53) Strasser, P.; Lübke, M.; Raspel, F.; Eiswirth, M.; Ertl, G. *J. Chem. Phys.* **1997**, *107*, 979.

(54) Mukouyama, Y.; Nakanishi, S.; Konishi, H.; Ikeshima, Y.; Nakato, Y. *J. Phys. Chem. B.* **2001**, *105*, 10905.

(55) Li, Z.L.; Ren, B.; Xiao, X.M.; Zeng, Y.; Chu, X.; Tian, Z.Q.; *J. Phys. Chem. A.* **2002**, *106*, 6570.

(56) Li, Z.L.; Cai, J.L.; Zhou, S.M. *J. Chem. Soc. Faraday Trans.* **1997**, *19*, 3519.

(57) Sagués, F.; Epstein, I.R. *Dalton Trans.* **2003**, *7*, 1201.

(58) Koper, M.T.M. *J. Chem. Soc. Faraday Trans.* **1998**, *94*, 1369.

(59) Krischer, K. *Advances in Electrochemical Science and Engineering* Alkire, R.C. Kolb, D.M. (Eds.) Wiley, **2003**, *2*, 8.

(60) Strasser, P. *Interface*, **2000**, 46.

(61) Wojtowicz, J. *Modern Aspects of Electrochemistry* Bockris, J.; Conway, B.E. (Eds.) Butterworths, London, **1973**, *8*, 47.

(62) Strasser, P.; Eiswirth, M.; Koper, M.T.M. *J. Electroanal. Chem.* **1999**, *478*, 50.

(80) Bard, A.J.; Faulkner, L.R. *Electrochemical Methods: Fundamentals and Applications 2nd Ed.* John Wiley & Sons, New York, **2001**.

(81) Retter, U.; Lohse, H. *Electroanalytical Methods: Guide to Experiments and Applications* Scholz, F. (Ed.), Springer-Verlag, Berlin, **2002**, 149.

(82) Autolab Electrochemical Instruments *Theory and Practical Aspects of Electrochemical Impedance Measurements* Application Note.

(83) Princeton Applied Research *Basics of Electrochemical Impedance Spectroscopy* Application Note AC-1.

(84) Popkirov, G.; Schindler, R. *Rev. Sci. Instrum.* **1993**, *64*, 3111.

(85) Weaver, M.J.; Chang, S.G. Leung, L.W.H.; Jiang, X. *J. Electroanal. Chem.* **1992**, *327*, 247.

(86) Sun, S-G. ; Chen, A.; Huang, T.; Li, J.; Tian, Z.W. *J. Electroanal. Chem.* **1992**, *340*, 213.

(87) Park, S.; Xie, Y.; Weaver, M.J. *Langmuir* **2002**, *18*, 5792.

(88) Liu, Z.L.; Ling, X.Y.; Su, X.D.; Lee, J.Y. *J. Phys. Chem. B.* **2004**, *108*, 8234.

(89) Li, W.Z.; Liang, C.H.; Zhou, W.J.; Qui, J.S.; Zhou, Z.H. *J. Phys. Chem. B.* **2003**, *107*, 6292.

(90) M.D. Vaudin, J. Res. Natl. Inst. Stand. Technol. 106 (2001) 1063.

(91) Gasteiger, H.A.; Marković, N.; Jr. Ross, P.N.; Cairns, E.J. *J. Phys. Chem.* **1993**, *97*, 12020.

(92) Park, S.; Wieckowski, A.; Weaver, M.J. *J. Am. Chem. Soc.* **2003**, *125*, 2282.

(93) Gasteiger, H.A.; Marković, N.; Jr. Ross, P.N.; Cairns, E.J. *J. Phys. Chem.* **1994**, *98*, 617-625.

(94) Kardash, D.; Korzeniewski, C. *Langmuir* **2000**, *16*, 8419.

(95) Comninellis, C.H.; Vercesi, G.P. *J. Appl. Electrochem.* **1991**, *21*, 335.

(96) Szynkarczuk, J.; Komorowski, P.G.; Donini, J.C. *Electrochimica Acta*, **1995**, *40*, 487.

(97) Melnick, R.E.; Palmore, G.T.R. *J. Phys. Chem. B.* **2001**, *105*, 9449.

(98) Melnick, R.E.; Palmore, G.T.R. *J. Phys. Chem. B.* **2001**, *105*, 1012.